ANNUAL REVIEWS

Annual Review of Fluid Mechanics

Predicting the Drag of Rough Surfaces

Daniel Chung,[1] Nicholas Hutchins,[1] Michael P. Schultz,[2] and Karen A. Flack[3]

[1]Department of Mechanical Engineering, University of Melbourne, Parkville, Victoria 3010, Australia; email: daniel.chung@unimelb.edu.au, nhu@unimelb.edu.au

[2]Department of Naval Architecture and Ocean Engineering, US Naval Academy, Annapolis, Maryland 21402, USA

[3]Department of Mechanical Engineering, US Naval Academy, Annapolis, Maryland 21402, USA

Annu. Rev. Fluid Mech. 2021. 53:439–71

The *Annual Review of Fluid Mechanics* is online at fluid.annualreviews.org

https://doi.org/10.1146/annurev-fluid-062520-115127

Keywords

roughness, wall turbulence, drag

Abstract

Reliable full-scale prediction of drag due to rough wall-bounded turbulent fluid flow remains a challenge. Currently, the uncertainty is at least 10%, with consequences, for example, on energy and transport applications exceeding billions of dollars per year. The crux of the difficulty is the large number of relevant roughness topographies and the high cost of testing each topography, but computational and experimental advances in the last decade or so have been lowering these barriers. In light of these advances, here we review the underpinnings and limits of relationships between roughness topography and drag behavior, focusing on canonical and fully turbulent incompressible flow over rigid roughness. These advances are beginning to spill over into multiphysical areas of roughness, such as heat transfer, and promise broad increases in predictive reliability.

1. PREVALENCE AND IMPORTANCE OF SURFACE ROUGHNESS

In fluid mechanics, whether a surface is smooth or rough is judged not in microns but by the flow occurring next to it. For a turbulent flow, a surface cannot be considered smooth if its topographical features are large enough to disrupt the smallest eddies near the wall and thus alter the transfer of momentum (drag), heat, and mass. In practice, this condition translates to topographical features greater than about 10 μm on both passenger aircraft and container ship hulls, about 1 μm on gas turbine blades, and about 0.1 mm on atmospheric surfaces. In this hydraulic (or aerodynamic) sense, all of the aforementioned examples are rough or nearly rough, with consequences for costs and emissions.

The basic problem (Section 2) is to predict performance-critical quantities such as drag and heat transfer, but because each roughness topography affects flow differently, routine predictions currently remain insufficiently reliable, with uncertainties costing billions of dollars per year (see the sidebar titled Economic Value of Uncertainty in Full-Scale Drag Predictions). As such, roughness continues to be an active area of research. The challenge in research has been the large number of relevant topographies and the costs associated with testing each topography, but these barriers have been lowered since the last major review of the subject (Jiménez 2004). The maturing of high-fidelity simulations and rapid-prototyping technologies as viable tools has permitted investigations of a growing array of roughness topographies with unprecedented levels of detail and accuracy (Section 4). These studies have enabled efforts to systematically unpick the effects of different topographical characteristics (Section 3) and to explore the far reaches of the Moody chart, yielding insights into limiting behaviors (Section 5). Progress is now at hand in challenging areas such as rough-wall heat transfer (Section 6). Here we highlight these recent advances, focusing on the prediction of drag and heat transfer due to rough wall-bounded turbulent flow, complementing recent reviews on predictive correlations (Flack & Schultz 2010) and outer-layer similarity (Flack & Schultz 2014). We also draw parallels with canopies, which constitute a specialized area focusing on dense roughness (Finnigan 2000, Nepf 2012), and we occasionally refer to engineered surfaces for drag reduction, which tend to be transitionally rough and are reviewed in depth elsewhere (García-Mayoral et al. 2019).

Roughness size: k is a roughness height, the choice of which is determined by application and context

Wall distance: without loss of generality, the origin of the y (wall-normal) coordinate is aligned with minimum roughness elevation; $y = 0$ is distinct from the zero-plane displacement of turbulence, $y = d$

Fluid properties: ν is the kinematic viscosity, α is the thermal diffusivity, ρ is the density, and c_p is the specific heat at constant pressure

Friction velocity: $u_\tau \equiv (\tau_w/\rho)^{1/2}$, where τ_w is the wall shear stress (drag per unit plan area) and ρ is the fluid density

Friction temperature: $\theta_\tau \equiv q_w/(\rho c_p u_\tau)$, where q_w is the wall heat flux (heat transfer per unit plan area), u_τ is the friction velocity, and ρ and c_p are fluid properties

$^+$ superscript: denotes viscous-friction scaling, where variables are scaled by u_τ, θ_τ, and ν; e.g., $U^+ \equiv U/u_\tau$, $\Theta^+ \equiv \Theta/\theta_\tau$, and $y^+ \equiv yu_\tau/\nu$

2. ACCOUNTING FOR ROUGHNESS IN TURBULENT FLOW

We first summarize the roughness problem (**Figure 1**). We would like to predict the drag per unit plan area, τ_w (SI units: N/m^2), or heat transfer per unit plan area, q_w (SI units: W/m^2), given any roughness topography characterized by its roughness size, k; flow at wall distance y characterized by the mean velocity, $U(y)$, and mean temperature, $\Theta(y)$, relative to the wall; and fluid properties, ν, α, ρ, and c_p. In dimensionless form, the problem can be stated as finding $\tau_w/(\rho U^2/2) = 2/U^{+2}$ and $q_w/(\rho c_p U\Theta) = 1/(U^+\Theta^+)$ as a function of y^+, k^+, and Pr, where the friction-scaled mean velocity is $U^+ \equiv U/u_\tau$, the friction-scaled mean temperature is $\Theta^+ \equiv \Theta/\theta_\tau$, u_τ is the friction velocity, θ_τ is the friction temperature, the viscous-scaled wall distance is $y^+ \equiv yu_\tau/\nu$, the roughness Reynolds number is $k^+ \equiv ku_\tau/\nu$, and the Prandtl number is $Pr \equiv \nu/\alpha$. Here, the $^+$ superscript denotes viscous-friction scaling. Use of the (total) plan area, A_t, as opposed to, e.g., the wetted area, A_w, allows for comparisons between surfaces at matched wall-normal fluxes of momentum and heat in the flow. We restrict the discussion to rigid roughness under canonical and fully turbulent incompressible flow and to forced convection where buoyancy is unimportant such that temperature variations behave as a passive scalar. Low solid conductivity [high roughness Biot number (Stimpson et al. 2017)] alters heat transfer, as the wall temperature would vary noticeably along roughness elements (Orlandi et al. 2016), but here we simplify the discussion by considering isothermal walls. The mass-transfer problem can be similarly posed (e.g., Brutsaert 1982).

ECONOMIC VALUE OF UNCERTAINTY IN FULL-SCALE DRAG PREDICTIONS

Improved drag predictions allow for better-informed and better-timed decisions. The translation between cost and drag is complex and involves socioeconomic aspects, such as emissions. In order to demonstrate the scale of the cost with traceable numbers, we provide the following simplified analysis based on energy considerations. The analysis merely reflects today's uncertainty in predicting drag due to roughness, not the drag penalty itself due to roughness, which would be even greater.

We use the scatter in k_s/k (Section 2.2.2) or ΔU^+ (Section 2.2.1) as a measure of what we cannot explain today, which could, in principle, be reduced with further research. To account for established topographical factors, we inspect the $k_s/(C_D k)$ versus λ_f data compilation in figure 1*a* of Jiménez (2004) to estimate that the scatter of k_s/k is 0.7 to 3, which is on the same order as that in the data compilation of k_s/k_{rms} versus Sk (Flack et al. 2019, figure 6). The fully rough approximation (Equation 3) translates this scatter in k_s/k to a range in ΔU^+ of $(1/\kappa)\ln 0.7 \approx -0.89$ to $(1/\kappa)\ln 3 \approx 2.7$, say ± 2, consistent with the scatter in figure 13 of Chan et al. (2015). The percentage scatter in drag coefficient $C_f \equiv 2/U_\delta^{+}$ at matched δ^+ (nominally smooth) or matched δ/k (nominally rough) can then be estimated using $\Delta C_f/C_f = (1 - \Delta U^+/U_\delta^+)^{-2} - 1 \sim 2\Delta U^+/U_\delta^+$, where U_δ^+ is based on the nominal condition. For many applications, including aircraft and ships, we have $U_\delta^+ \approx 20$–35, meaning that the uncertainty in full-scale drag prediction, $\Delta C_f/C_f$, is at least $2(\pm 2)/35 \approx \pm 11\%$. This estimate, of course, depends on having a well-behaved surface that obeys the framework in Section 2. The practice of setting $k_s = k$ should be discouraged because it corresponds to a potential error of at least 0.1 to 10 of the actual k_s/k (Jiménez 2004, figure 1*a*), or ± 6 in ΔU^+, which, in turn, translates to an uncertainty in $\Delta C_f/C_f$ of at least $2(\pm 6)/35 \approx \pm 34\%$.

In shipping, skin friction can account for up to 90% of the drag (Schultz et al. 2011). Due to the ban on coatings containing TBT (tributyltin), ship hulls routinely develop slime films (Schultz et al. 2015). The cost of this type of moderate hull fouling for the US Navy's Arleigh Burke-class destroyer fleet alone is estimated to amount to over US$1 billion over 15 years, primarily due to increased fuel consumption to overcome the ≈10% drag penalty (Schultz et al. 2011). In-water hull cleanings can significantly reduce this roughness impact, but economically informed maintenance decisions depend on accurate drag estimates. If the wetted hull area of this class represents 22% of the fleet, and the fleet represents 0.5% of the number of ships globally (cf. Schultz et al. 2011), then scaling the ≈10% drag penalty by the ±11% drag uncertainty due to roughness yields a corresponding uncertainty of ±US$67 billion per year globally.

In aviation, where skin friction constitutes 50% of drag (Spalart & McLean 2011) and fuel costs are six times the global profits in 2018 (IATA 2019), the ±11% drag uncertainty, such as for acoustic-liner roughness in fan ducts [$k_s \approx 20$ μm, ≈6% of the skin-friction wetted area (cf. Spalart et al. 2017)], here amounts to ±2% of profits. For the nominally smooth but nearly rough aircraft skin [$k_s \approx 10$ μm (Moyes et al. 2017)], the +11% skin-friction uncertainty due to roughness translates to a drag penalty of 5.5%, or 33% of profits.

Roughness is routinely considered when siting wind farms using classifications mapped to standardized values of y_0. Given the wind speed U_{10} at $y = 10$ m from meteorological data, the available power, which scales with the cube of U_{100} at the typical turbine hub height of $y = 100$ m, can be estimated using the log law $U_{100}^3 \approx U_{10}^3[\ln(100\text{ m}/y_0)/\ln(10\text{ m}/y_0)]^3$. Taking $y_0 = 0.01$ m of tall grass (Stevens & Meneveau 2017) as an example, an error bar of 0.7 to 3 of y_0, consistent with that of k_s, corresponds to an uncertainty due to roughness in available power of ≈ ±9%, which affects turbine selection and economic viability.

The formulation here using y, U, and Θ is natural for large-eddy simulation (LES) wall models or Reynolds-averaged Navier–Stokes (RANS) wall functions, but the basic structure and response are preserved if the problem is posed, for pipe or channel flows of cross section $\int \mathrm{d}A$, using the bulk velocity $U_b \equiv \int U\,\mathrm{d}A/\int \mathrm{d}A$, mixed-mean temperature $\Theta_m \equiv \int U\Theta\,\mathrm{d}A/\int U\,\mathrm{d}A$ and pipe radius or half-channel height δ (Moody 1944, Nikuradse 1933, Dipprey & Sabersky 1963), or, for

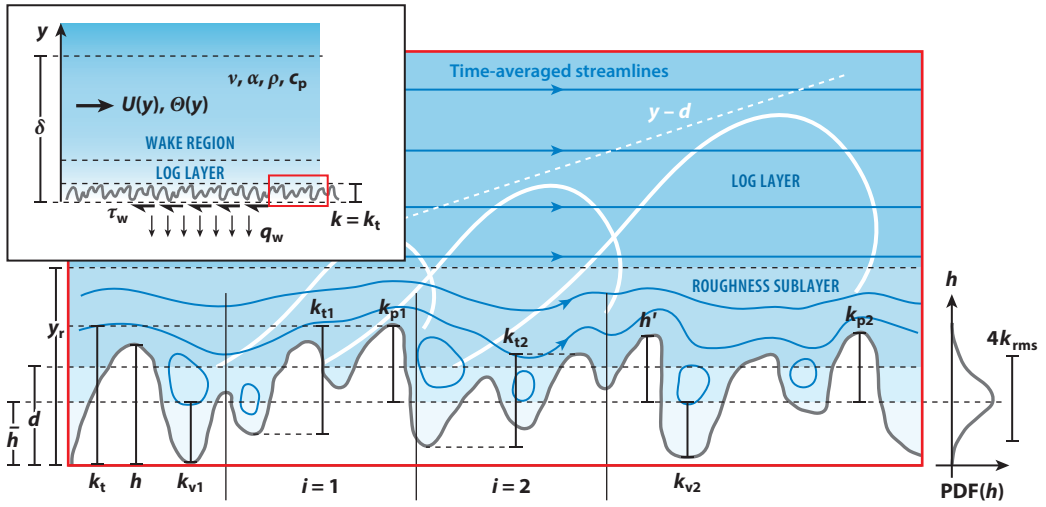

Figure 1

(*Inset*) The setup of the roughness problem. The desired outputs are the wall shear stress, τ_w, or the wall heat flux, q_w, given the mean velocity, $U(y)$, and mean temperature, $\Theta(y)$, at distance y from the wall, along with fluid properties ν, α, ρ, and c_p. The wall is characterized by a physical roughness size, k, here chosen to be the maximum peak-to-trough roughness height, k_t (Section 3.1.1), and δ is the outer-layer thickness (e.g., boundary-layer thickness). For concreteness, the wall-normal coordinate $y = 0$ is aligned with the minimum roughness elevation. (*Main figure*) A close-up view of the rectangular region of roughness topography in the inset. Here, h describes the roughness topography. The average roughness elevation is located at $y = \overline{h}$, from which the variation h' is measured. The peak-to-trough roughness height of subsample i is k_{ti}. The height above $\overline{h}$ of the ith-highest peak of the entire sample is k_{pi} and the depth below $\overline{h}$ of the ith-lowest trough of the entire sample is k_{vi}. Above the roughness sublayer (Section 2.1.2) ($y > y_r$), the time-averaged flow (*blue streamlines*) is spatially homogeneous. The wall offset (zero-plane displacement) (Section 2.1.1) is located at $y = d$ such that $y - d$ is the distance-to-the-wall scale of the turbulent eddies (*solid white lines*) in the log layer: $y_r < y \ll \delta$. A notional probability density function (PDF) of h is shown on the right, along with a measure of its width, k_{rms}, where k_{rms} is the root-mean-square of h' or, equivalently, the standard deviation of h.

boundary layers, using the freestream velocity $U_\delta \equiv U(y = \delta)$ and temperature $\Theta_\delta \equiv \Theta(y = \delta)$ and boundary-layer thickness δ or fetch x (Prandtl & Schlichting 1934, Granville 1958, Yaglom 1979) (cf. Section 2.3). Thus, in all formulations, knowledge of the mean velocity and temperature profiles for the wall-bounded turbulence formed over a rough surface, $U^+(y^+; k^+)$ and $\Theta^+(y^+; k^+, Pr)$, respectively, is akin to solving the problem of drag τ_w and heat transfer q_w of rough surfaces.

Viscous wall unit: a length ν/u_τ above a smooth wall that scales the viscous sublayer and the smallest eddies of turbulent flow

Roughness sublayer: in principle, the near-wall region $y < y_r$ that knows about the roughness topography; above it, the time-averaged flow is spatially homogeneous

2.1. Outer-Layer Similarity

All predictive models rely on an important assumption, proposed by Townsend (1956, p. 89) and articulated by Raupach et al. (1991), that smooth- and rough-wall turbulence behave similarly away from the wall. Specifically, this similarity hypothesis states that friction-scaled turbulent relative motions in the outer layer ($\delta \geq y \gg \nu/u_\tau$, k), such as the mean velocity defect $U_\delta^+ - U^+$ and covariances of velocity fluctuations $\overline{u_i' u_j'}^+$, are independent of surface condition at sufficiently high Reynolds number (i.e., when the outer-layer thickness is greater than the viscous wall unit, $\delta \gg \nu/u_\tau$) and sufficiently large scale separation ($\delta \gg k$). The direct effect of roughness is confined to the roughness sublayer ($y < y_r$), and roughness only sets the boundary condition, namely the friction velocity u_τ for the outer flow of thickness δ. This is basically a dimensional argument that implies that only u_τ and δ are relevant in the outer layer, from which we obtain, e.g., $U_\delta - U = u_\tau F(y/\delta)$ and $\overline{u_i' u_j'} = u_\tau^2 G_{ij}(y/\delta)$, where F and G_{ij} are each unique functions of y/δ, independent of whether the wall is smooth or rough.

EQUIVALENT SAND-GRAIN ROUGHNESS

Inspired by the pioneering studies of Nikuradse (1933), Schlichting (1937) introduced the concept of the equivalent sand-grain roughness k_s of a surface, which defines the grain size of uniform (monodisperse), close-packed sand grains on a hypothetical surface that would cause the same drag as the surface of interest if exposed to the same flow in the fully rough regime (Section 2.2.2). Although it is a length scale, k_s does not measure a physical distance. Rather, it is a hydraulic scale defined by drag that must be determined from experiments or simulations for a specific surface roughness. This is the roughness height listed on the Moody diagram (Moody 1944), providing a common currency (Bradshaw 2000) across disparate roughness for wall-bounded turbulence and serving as an input parameter for predictions, e.g., RANS calculations and rough flat plate calculations (Section 2.3). The simplicity of this single parameter masks its complicated origin, and the potential exists to incorrectly use k_s as a physical measure of roughness elevation, or to incorrectly ascribe k_s based on geometry.

The general validity of this hypothesis for a wide range of roughnesses is tied to the stated or unstated assumptions above. For example, an unstated assumption that is easy to overlook is the necessity that not just k but also no other surface scales compete with y and δ for relevance in the outer layer (or else F and G_{ij} would not be functions of only y/δ), noting that a single scale k by itself is insufficient to fully describe any roughness topography. Such cases are not necessarily academic but often arise in practice (Section 5). An often-quoted criterion for the necessary separation of scales is $k/\delta < 1/40$ (Jiménez 2004), which is based on the assumption that roughness directly influences up to $y_r = 3k$ of the flow above it so that restricting this region to be below half of the thickness of the log layer, i.e., $3k < 0.5 \times 0.15\delta$, leads to $k/\delta < 1/40$. But for roughness with in-plane features of wavelength much larger than k, the direct region of influence could be larger than $y_r = 3k$ (Section 2.1.2), and the quoted scale separation k/δ should correspondingly be smaller than 1/40. Because these kinds of cases challenge the validity of our classical understanding outlined above, with consequences for the reliability of prediction, several roughness studies (e.g., Flack et al. 2005, Castro 2007, Amir & Castro 2011, Krogstad & Efros 2012) have been dedicated to assessing and revisiting these cases, as reviewed by Flack & Schultz (2014), the consensus being that outer-layer similarity does hold once a sufficiently large scale separation is achieved, even for two-dimensional (2D) roughness such as tranverse bars and rods (Krogstad & Efros 2012). It is difficult to prescribe guarantees of outer-layer similarity, but if in doubt, checks at higher δ/k and fixed k^+ are recommended (e.g., Leonardi et al. 2007). Accurate wall shear stress, a notoriously difficult quantity to measure experimentally, is critical for assessing outer-layer similarity. Depending on the facility and operating flow conditions, the accuracy of u_τ can be, for boundary layers, $\approx\pm 4\%$ using indirect methods (Schultz & Flack 2007) and $\approx\pm 1$–3% using drag balances (Krogstad & Efros 2010, Squire et al. 2016) and, for channels, $\approx\pm 0.5$–4% from measurement of pressure drop (Schultz & Flack 2013).

Two-dimensional (2D) roughness: 2D roughness denotes topographies with variation only in one direction, while 3D roughness denotes topographies with both streamwise and spanwise variations, i.e., $h' = h'(x, z)$

2.1.1. Wall offset ($y = d$). An important aspect to consider when assessing outer-layer similarity is the zero-plane displacement, d, also known as the wall offset. The distance y is often measured from a reference plane, such as the bed on which roughness elements are mounted. However, the outer turbulent flow does not perceive its origin to be at $y = 0$ but at $y = d$ (**Figure 1**). The shifted wall-normal coordinate $y - d$ corrects for this flow-physical inconsistency so as to collapse all profiles in the outer layer: $U_\delta - U = u_\tau F[(y - d)/(\delta - d)]$ and $\overline{u_i' u_j'} = u_\tau^2 G_{ij}[(y - d)/(\delta - d)]$. A similar concept is the canopy penetration depth, $\epsilon \equiv k - d$ (Luhar et al. 2008, Nepf 2012), where k is the height of the canopy. For small k^+, $y = d$ locates the mostly intact smooth-wall-like turbulence

Sparse or dense regime: the drag behavior with increasing frontal solidity λ_f (at fixed or varying plan solidity λ_p): k_s/k increases in the sparse regime but decreases in the dense regime

that is displaced relative to the mean flow such that $U(y = d)$ is nonzero, a concept that can be exploited to reduce drag (Luchini et al. 1991, Bechert et al. 1997, Jiménez 2004, García-Mayoral et al. 2019). For larger k^+, the near-wall turbulence is altered, and d locates the extrapolation to zero of the distance-to-the-wall scaling $y - d$ of the turbulence (**Figure 1**) that is associated with the log profiles (Section 2.2) (Nikora et al. 2002). In general, $U(y = d)$ is not necessarily 0. The offset $y = d$ is typically between the crest and trough of roughness elements, and depends not only on the roughness topography but also on the roughness Reynolds number. For roughness in the sparse or dense regime, $y = d$ approaches the crest or the trough, respectively (Jackson 1981, Raupach et al. 1991, Macdonald et al. 1998, Grimmond & Oke 1999, Luhar et al. 2008). If the spacing between roughness elements is small relative to viscous scales, $y = d$ also approaches the crest because the flow behaves as if a smooth wall were located at the crest (MacDonald et al. 2016, 2018; Sharma & García-Mayoral 2020). Far above the roughness ($y \gg k$), the offset $0 < d < k$ is often neglected, where $y = k$ is the crest of the roughness, and so $y - d \sim y$ is valid for cases with large scale separation ($\delta \gg k$) and thus large Reynolds numbers ($\delta \gg \nu/u_\tau$) since we have $\delta > y \gg k \gtrsim \nu/u_\tau$ for rough walls. In the log layer above, for example, a fully rough wall (Section 2.2), for $y/k \gg 1$, say $y/k = \mathcal{O}(10)$, and $k_s = \mathcal{O}(k)$, the error incurred in assessing the mean profile, $U^+ = (1/\kappa)\ln[(y - d)/k_s] + B_s(\infty)$, is the discrepancy $(1/\kappa)\ln[1 + \mathcal{O}(0.1)] \approx 0.24$, which is small relative to $U^+ = (1/\kappa)\ln[\mathcal{O}(10)] + B_s(\infty) \approx 14$ ($0.24/14 \approx 1.7\%$). For some applications, such as dense canopies, the wall offset can be close to the crest of the roughness ($d \approx k$) and $k_s/k \ll 1$ (say 0.1; see Luhar et al. 2008). In such cases, a log region can be well established close to the roughness crests $y/k \gtrsim \mathcal{O}(1)$ (say, $y/k = 3$) owing to sufficient scale separation, $y - d \gg k_s$ ($3k - k = 2k \gg 0.1k$ in this case), but where d cannot be neglected since it remains an appreciable proportion of y ($d/y = 1/3$ in this case).

Jackson (1981) proposed the center of drag as a way to locate the zero-plane displacement but this is not necessarily a reliable measure of the origin of turbulence that is associated with the log profiles. Indeed, it has been shown that this definition is not always appropriate (Cheng & Castro 2002, Breugem et al. 2006, Coceal et al. 2007, Chan-Braun et al. 2011, Chan et al. 2015, MacDonald et al. 2018). The analysis of Jackson (1981) assumes zero pressure gradient and fully developed flow, which are perfectly satisfied in neither boundary-layer nor internal pressure–driven flows. Internal flows with a large volume of obstruction relative to the outer-layer thickness are susceptible to this bias (Breugem et al. 2006, Pokrajac et al. 2006, MacDonald et al. 2018), and a simple extension to include pressure gradients seems unsatisfactory (Breugem et al. 2006). In summary, the offset d is a parameter determined by the flow (like the equivalent sand-grain roughness, k_s; Section 2.2.2). Geometrical definitions (e.g., mean roughness elevation, $\overline{h}$; Chan et al. 2015) are well defined, but the wall offset needs to be accounted for in denser topographies. If the log law does not exist, e.g., in the case of insufficient scale separation, then other definitions may be better suited (Nikora et al. 2002).

2.1.2. Roughness sublayer ($y < y_r$). Each roughness topography has a specific flow signature near the wall. For example, the flow can resemble flow over bluff bodies, including separated flow with reattachment regions and shed vortices (Hong et al. 2011, Yuan & Piomelli 2014b). This roughness-affected region near the wall is labeled the roughness sublayer ($y < y_r$), the extent of which is roughness dependent. In this region, one of the assumptions of outer-layer similarity (a condition for the log law) is violated ($y \not\gg k$) and the flow is clearly influenced by the local roughness topography. In principle, $y > y_r$ quantifies the scaling argument $y \gg k$ where outer-layer similarity holds. In practice, even though similarity of the mean recovers above $y_r \gtrsim k$, i.e., without a large scale separation, similarity of the turbulent fluctuations requires a large scale separation and also depends on the scale of the fluctuations (Flack & Schultz 2014, Chan et al. 2018) and

roughness type (e.g., 2D bars; Flack & Schultz 2014). A measure of the roughness sublayer (of the mean) can be determined by the wall-normal location y_r above which the time-averaged flow is spatially homogeneous, as set by a threshold (Raupach et al. 1980, Pokrajac et al. 2007; see also the time-averaged streamlines in **Figure 1**).

In-plane roughness wavelength: λ is an in-plane scale of the roughness topography, e.g., lateral or streamwise inter-element spacing or wavelength, the choice of which is determined by application and context

It is convenient to quote the wall-normal extent of the roughness sublayer based on a roughness topographical feature. Jiménez (2004) and Raupach et al. (1991) suggest two to five times k but it is not obvious which roughness height k to use in general. Assessing similarity of the turbulent fluctuations, Flack et al. (2007) proposed $3k_s$ as the height of the roughness sublayer, using the hydraulic scale, k_s (Section 2.2.2). The advantage to using k_s is that it incorporates the drag-producing surface features for defining the roughness sublayer, but the disadvantage is that it can no longer be determined from topography. In a study of 3D sinusoidal roughness for a range of height-to-wavelength ratios, Chan et al. (2018) found $y_r \propto \lambda \approx 0.5\lambda$, where λ is the in-plane roughness wavelength, rather than $y_r \propto k$, provided that the zero-plane displacement d is accounted for, i.e., $y_r \approx d + 0.5\lambda$, which is particularly important for the denser sinusoids, for which d approaches the crest. This scaling is also observed for 3D canopies (Sharma & García-Mayoral 2020) and is consistent with the emergent literature on spanwise heterogeneous roughness (Section 5.2.2), where the wall-normal extent of the secondary flows is proportional to the spanwise wavelength of heterogeneity, Λ. A similar scaling, $y_r \approx k + \lambda$, was pointed out by Raupach et al. (1980), with λ identified as the spanwise spacing (Raupach et al. 1991). For infinitely wide (2D) surfaces, the streamwise spacing must be considered (Jiménez 2004). Lee & Sung (2007) studied $k \times k$ bars with pitch $\lambda = 8k$, finding $y_r \approx 5k$.

2.2. Log Laws

In turbulent wall-bounded flow over smooth walls, ν/u_τ scales the viscous sublayer, and when the roughness size k is small relative to this scale, i.e., $k^+ \ll 1$, the roughness is submerged below the viscous sublayer and the surface appears smooth to the flow. If the outer Reynolds number is sufficiently large ($\delta \gg \nu/u_\tau$), an inertial range of y where viscosity does not directly matter ($y \gg \nu/u_\tau$) can emerge near the wall that is independent of the outer-flow geometry ($y \ll \delta$). There, the only dimensionless group involving the mean velocity gradient is $(y/u_\tau)(\mathrm{d}U/\mathrm{d}y) = 1/\kappa$, where κ ($\approx$0.4) is the von Kármán constant. Integration leads to the textbook log law,

$$U_S^+ = (1/\kappa)\ln y^+ + A, \qquad 1.$$

where the log-law intercept A ($\approx$5.0) is universal for smooth walls ($k^+ \ll 1$) and the subscript "S" indicates smooth-wall conditions. The intercept A is like a boundary condition because it is the value of U^+ if the log law is extrapolated to $y^+ = 1$. When the wall is rough such that k^+ is no longer small, the additional requirement that y is far above the direct influence of roughness ($y/k \gg 1$), i.e., above the roughness sublayer, leads to the same sole-surviving dimensionless group as in the case of the smooth wall, $(y/u_\tau)(\mathrm{d}U/\mathrm{d}y) = 1/\kappa$, but the integration constant is now B in y/k coordinates:

$$U_R^+ = (1/\kappa)\ln(y/k) + B(k^+), \qquad 2.$$

where B is a function of both the roughness topography and the roughness Reynolds number k^+ and the subscript "R" indicates rough-wall conditions. If viscous effects can be neglected in setting the intercept B, then for $k^+ \gg 1$ the intercept B approaches a finite value $B(\infty)$ that is independent of roughness Reynolds number but depends only on the roughness topography. The converse is not always true, i.e., it does not always follow that viscous effects can be neglected given $k^+ \gg 1$, e.g., large riblets (Gatti et al. 2020).

Outer-layer similarity ($y \gg \nu/u_\tau$, k) is one necessary condition to obtain the log laws of Equations 1 and 2. For this reason, the appearance of a log law has often been taken as evidence of outer-layer similarity. However, an additional condition for logarithmic behavior is $y \ll \delta$, while Townsend's outer-layer similarity requires only $y < \delta$. These requirements relate to the roughness sublayer, y_r. The existence of a log region in rough-wall flows requires $y > y_r$ and $y \ll \delta$, which are void when $y_r/\delta \not\ll 1$. Even in these scenarios, outer-layer similarity remains a possibility beyond and without the log region, in the limited wake region $y_r < y < \delta$. Presumably, studies (Castro 2007, Amir & Castro 2011, Chan et al. 2015) observing that outer-layer similarity holds even for $k/\delta \gtrsim 0.15$ are referring to this kind of similarity in the wake. This is the so-called obstacle regime (Jiménez 2004) of large relative roughness (Flack & Schultz 2014) in which the log-law parameters κ, A, and $B(k^+)$ are not well apparent.

Equation 2 provides an expression for $U^+(y^+; k^+)$, and so the effect of a given rough surface boils down to determining the unknown function, $B(k^+)$. All of the physical dimensional reasoning has already been made leading up to Equations 1 and 2. Hereafter, discussions in terms of the roughness function ΔU^+ (Section 2.2.1), equivalent sand-grain roughness k_s (Section 2.2.2), roughness length y_0 (Section 2.2.3) or drag length $(C_D a)^{-1}$ (Section 5.1) are a matter of taste, convention, interpretation, convenience, or history. For precision, y should be replaced by $y - d$ near the roughness in Equation 2 to account for the offset of the turbulent flow (Section 2.1.1).

Wake: in wall-bounded turbulence, the departure of the mean velocity profile, $U(y)$, from the log law in the outer layer, $y \gtrsim 0.15\delta$

Skin-friction coefficient: $C_f \equiv \tau_w/(\frac{1}{2}\rho U_\delta^2)$, where τ_w is the wall shear stress, ρ is the fluid density, and U_δ is the mean velocity U at $y = \delta$

Maximum peak-to-trough roughness height: $k_t \equiv \max(b') - \min(b')$, where b' is the variation in roughness elevation about the mean

Subsample-average peak-to-trough roughness height: $\bar{k}_t \equiv \frac{1}{N}\sum_{i=1}^{N} k_{ti}$, where k_{ti} is the peak-to-trough height of the ith subsample

2.2.1. Roughness function, ΔU^+.

A convenient and intuitive way to describe the log-law intercept $B(k^+)$ is through the roughness function $\Delta U^+(k^+)$, defined independently by Clauser (1954) and Hama (1954) and given by the shift at matched y^+ of the rough-wall log law (Equation 2) relative to that of the smooth wall (Equation 1):

$$\Delta U^+(k^+) = U_S^+ - U_R^+ = (1/\kappa)\ln k^+ + A - B(k^+). \qquad 3.$$

The roughness function captures the momentum deficit resulting from surface roughness and thus can be interpreted as a measure of the drag penalty relative to a smooth wall: Drag increases for $\Delta U^+ > 0$ and drag reduces for $\Delta U^+ < 0$. The roughness function also expresses the difference in skin-friction coefficient between the smooth wall, C_{fS}, and the rough wall, C_{fR}, at matched δ^+ (**Figure 2*a***). The roughness function is invaluable in permitting experimental or numerical roughness data, often obtained at lower outer Reynolds numbers and in a particular geometry (e.g., pipe), to be scaled up to predict drag at application Reynolds numbers in other geometries (e.g., channel or flat plate) (Section 2.3). Some caution is required here since Chan et al. (2015) and Thakkar et al. (2018) have both noted that ΔU^+ retains some δ^+ dependence at low δ^+ (and low δ/k), due to a distorted log region that is not yet fully formed [cf. obstacles (Jiménez 2004)], but such effects are likely limited to $\delta^+ \lesssim 200$ (and $\delta/\bar{k}_t \lesssim 10$), overestimating ΔU^+ by $\lesssim 1$.

To appreciate the influence of a rough surface on wall-bounded turbulence, in **Figure 2*b*** we map ΔU^+ of a few surfaces as a function of roughness Reynolds number, $k^+ \equiv k u_\tau/\nu$, where $k = k_t$ or $\bar{k}_t$ presently (respectively, the maximum peak-to-trough roughness height or the subsample-average peak-to-trough roughness height). For $\Delta U^+ = 0$, the surface remains hydrodynamically smooth because viscosity damps out the roughness-induced turbulent fluctuations that would otherwise retard the flow. As k^+ increases, the onset of roughness effects occur, $\Delta U^+ \gtrsim 0$, and the flow is said to be transitionally rough. In this roughness regime, both viscous and pressure drag on the roughness elements contribute to skin friction. As k^+ increases further, pressure drag dominates, $\tau_w \propto \rho U^2$. In this so-called fully rough regime, the skin-friction coefficient (at constant k/δ) becomes independent of Reynolds number ($Re_\delta \equiv \delta U_\delta/\nu$; see **Figure 3*a***), and Equation 3 shows that ΔU^+ asymptotes to $(1/\kappa)\ln k^+ + A - B(\infty)$, where $B(\infty)$ is the

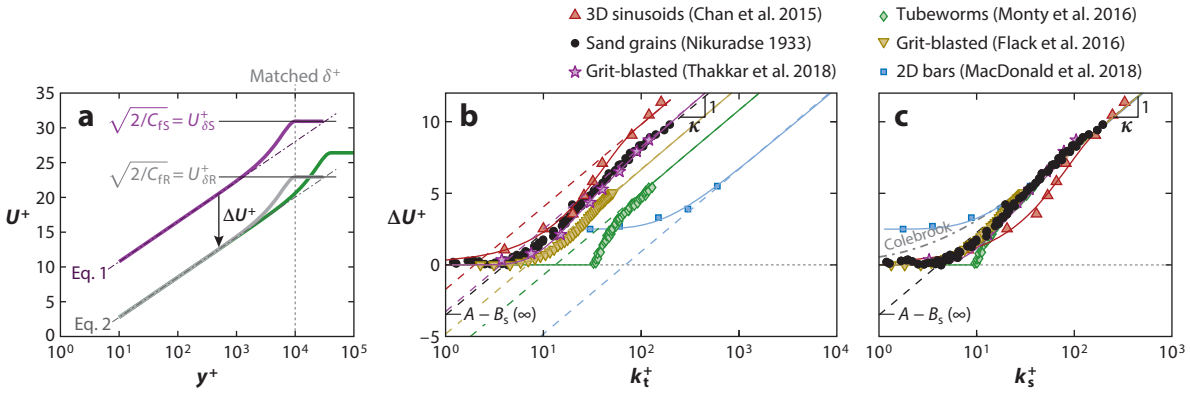

Figure 2

(*a*) Mean velocity profile, U^+, for (*purple curve*) smooth- and (*gray curve*) rough-wall turbulent boundary layers at matched δ^+, along with the rough-wall profile at higher δ^+ (*green curve*). Black and gray dot-dashed lines show Equations 1 and 2, respectively (the log laws for the smooth and rough profiles). (*b*) Roughness function ΔU^+ as a function of peak-to-trough roughness height, k_t^+ (see **Figure 1**), for various rough surfaces. For grit-blasted and tubeworm surfaces, the average peak-to-trough roughness height $\overline{k}_t$ is used. Dashed lines show Equation 3. (*c*) ΔU^+ as a function of equivalent sand-grain roughness, k_s^+. The dashed line shows Equation 4, and the dot-dashed line shows Colebrook's (1939) formulation for the roughness function.

finite log-law intercept that depends only on the roughness topography [indicated for sand-grain roughness $B_s(\infty)$ in **Figure 2*b***].

Every rough surface has a possibly distinct ΔU^+ (k^+), not only in the value of the fully rough intercept $B(\infty)$ but also in the behavior of the transitionally rough regime—this is what makes the prediction of drag due to rough surfaces so difficult. The Moody diagram (Moody 1944) adopts the Colebrook form (Colebrook 1939) of the friction factor, which is equivalent to the roughness function, $\Delta U^+ = (1/\kappa)\ln(1 + \gamma\, k^+)$ (cf. Grigson 1992, equation 15), with $\gamma \equiv \exp\{\kappa[A - B(\infty)]\}$. This

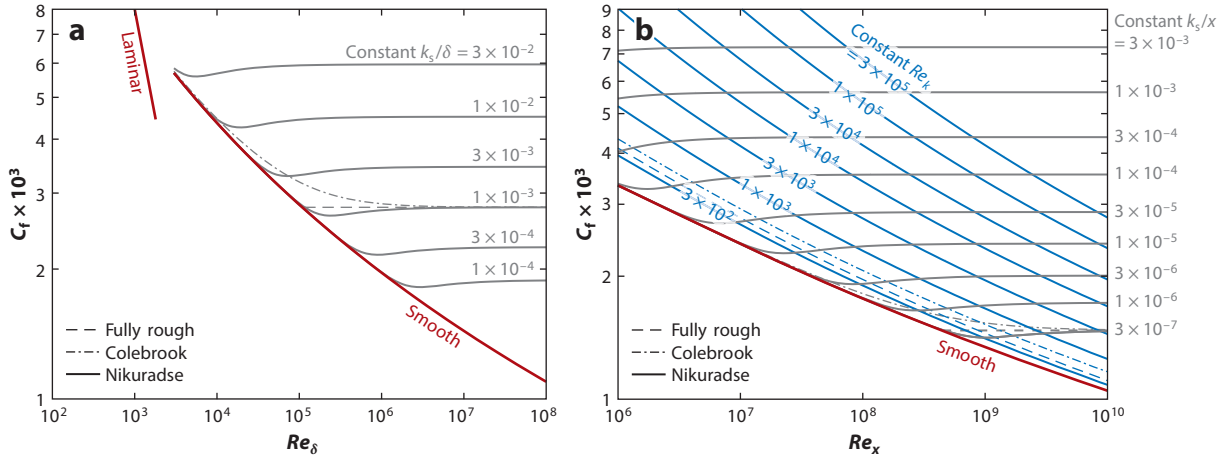

Figure 3

Full-scale predictions. (*a*) A Moody (1944)-type chart for a pipe [$\kappa = 0.4$, $A = 5$, $B_s(\infty) = 8.5$, and Π and W as given by Nagib & Chauhan (2008)]. Here, κ is the von Kármán constant, A is the smooth-wall intercept, $B_s(\infty)$ is Nikuradse's (1933) fully rough intercept for uniform sand grains, Π is the wake strength, and W is the wake function. (*b*) Drag curve for rough-wall boundary layers developing over a flat plate [$\kappa = 0.4$, $A = 5$, $B_s(\infty) = 8.5$, and Π and W as given by Monty et al. (2016)].

formulation is based on commercial pipes where wall drag displayed a gradual, monotonic transition from hydraulically smooth to fully rough behavior. This roughness function shape implies $\Delta U^+ > 0$ for all $k^+ > 0$, negating complete viscous damping of roughness-induced disturbances even for $k^+ \ll 1$ (this formulation is shown in **Figure 2*c***). This behavior stands in contrast to the abrupt departure from the hydraulically smooth condition ($\Delta U^+ = 0$ for finite values of k^+) and the inflectional nature of the skin friction in the transitionally rough regime observed by Nikuradse (1933) in classic pipe-flow experiments using uniform sand grains (**Figure 2*b*,*c***). Colebrook (1939) asserted that this difference in the transitionally rough regime stemmed from the uniformity of the roughness used by Nikuradse and the close-packed arrangement of the elements. Bradshaw (2000) provided a theoretical argument for Nikuradse- versus Colebrook-type behavior based on the Oseen solution for isolated roughness elements. However, recent data indicate that irregular, engineered surfaces with multiple scales of roughness more closely follow Nikuradse-type (critical onset) behavior than Colebrook-type behavior (gradual onset) (**Figure 2*c***). For instance, honed surfaces (Shockling et al. 2006, Schultz & Flack 2007), commercial steel pipes (Langelandsvik et al. 2008), painted and sanded surfaces (Flack et al. 2012), grit-blasted surfaces (Flack et al. 2016, Thakkar et al. 2018; **Figure 2*b*,*c***), and even sparsely biofouled surfaces (Monty et al. 2016; **Figure 2*b*,*c***) all exhibit sudden departure from the hydraulically smooth regime, and many also display inflectional C_f behavior in the transitionally rough regime. Bradshaw's (2000) argument is also at odds with that used for riblets (cf. Jiménez 2004, García-Mayoral et al. 2019). While ΔU^+ of most surfaces displays asymptotic $(1/\kappa)\ln k^+ +$ constant behavior in the fully rough regime, some surfaces have demonstrated a ΔU^+ that does not scale with roughness height (Sections 3.1.4 and 5).

Nikuradse- versus Colebrook-type: the shape of the roughness function ΔU^+ in the transitionally rough regime: Nikurase-type exhibits critical (on-or-off) behavior, while Colebrook-type exhibits gradual behavior

2.2.2. Equivalent sand-grain roughness height, k_s. If the roughness Reynolds number is based on the equivalent sand-grain roughness height, $k_s^+ \equiv k_s u_\tau/\nu$, then the roughness function (Equation 3) for all surfaces is set by

$$\Delta U^+(k_s^+) = (1/\kappa)\ln k_s^+ + A - B_s(k_s^+), \qquad 4.$$

where $B_s(k_s^+)$ is the unique log-law intercept function of U_R^+ (cf. Equation 2) measured by Nikuradse (1933) for uniform sand grains, which is the de facto standard. In the literature, $B_s(k_s^+)$ is typically presented as data or a fit, but the important value is the limit $B_s(\infty) = 8.5$ in the fully rough regime (such that the log intercept of Equation 4 in **Figure 2*b*,*c*** is $A - B_s(\infty) \approx 5.0 - 8.5 \approx -3.5$). Comparing Equations 3 and 4 in the fully rough regime, we can convert from the physical roughness size k to the hydraulic scale k_s, using $k_s/k = \exp\{\kappa[B_s(\infty) - B(\infty)]\}$, where $B_s(\infty)$ takes the standardized value of 8.5. This relationship, where k_s/k is determined by only κ and $B(\infty)$, is a consequence of the equivalent sand-grain roughness concept (cf. Schlichting 1937). Without the fully rough condition, B_s and B remain functions of k_s^+ and k^+, respectively, and matching Equations 3 and 4 yields a ratio k_s/k that is a function of k^+. To make explicit the often implied fully rough condition, researchers sometimes use the $k_{s\infty}/k$ notation for the constant (Jiménez 2004). Equation 4 is a useful way to determine k_s/k from ΔU^+. Graphically, this procedure is the same as shifting the horizontal log axis (multiplying k by a factor C) such that the fully rough asymptote (large k^+ data) collapses onto $\Delta U^+ = (1/\kappa)\ln(Ck^+) + A - B_s(\infty)$, the resulting shift C being just k_s/k (**Figure 2*c***). Practitioners should be cautious when comparing values for k_s/k or ΔU^+ across multiple studies, or when using these to make full-scale predictions, to ensure that there is consistency in κ, A, and $B_s(\infty)$.

2.2.3. Roughness length, y_0. Similar to k_s, the roughness length y_0 is used in meteorology, such that $U_R^+ = (1/\kappa)\ln(y/y_0)$, i.e., it is the location $y = y_0$ where the log law extrapolates to

$U^+ = 0$. As with Equation 2, y should be replaced with $y - d$ for $y = \mathcal{O}(k)$ to account for the wall offset (Section 2.1.1). Comparing Equations 2 and 3 gives $\Delta U^+ = (1/\kappa)\ln y_0^+ + A \Leftrightarrow y_0^+ = \exp[\kappa(\Delta U^+ - A)]$ (cf. Castro 2007). In the fully rough regime, matching the above with Equation 4 gives $y_0/k_s = \exp[-\kappa B_s(\infty)] \approx 1/30$, a good relationship to keep in mind.

2.3. Full-Scale Prediction

Full-scale predictions of the skin-friction coefficient C_f are possible via an assumed mean velocity profile, U^+. Writing Equation 2 in terms of k_s and adding a wake function W ($\equiv 2$ for $y = \delta$) of strength Π yield the following composite expression valid from the log region up to $y = \delta$:

$$U^+ = (1/\kappa)\ln(y/k_s) + B_s(k_s^+) + (\Pi/\kappa)W(y/\delta). \quad 5.$$

At the edge of the boundary layer, we have $y = \delta$ and $U^+ = U_\delta^+ \equiv \sqrt{2/C_f}$, so Equation 5 reduces to an implicit equation that can be solved, provided that we know B_s as a function of $k_s^+ = (k_s/\delta)Re_\delta/\sqrt{2/C_f}$, to find $C_f = C_f(k_s/\delta, Re_\delta)$, with $Re_\delta \equiv \delta U_\delta/\nu$. This is shown in **Figure 3*a***, which is essentially the commonly used Moody chart, only here we present C_f and Re_δ based on the center-line velocity, U_δ. With only a moderate increase in complexity we could repose the problem in terms of a (pipe) bulk velocity, $U_b = (1/\delta^2)\int_0^\delta 2U(\delta - y)\,dy$, and a friction factor, $8/(U_b^+)^2$ (Nikuradse 1933), as is common for internal geometries.

For a turbulent boundary layer developing over a flat plate (a model for a ship hull or an aircraft fuselage), the boundary-layer thickness δ is a function of the development length x and so, rather than k_s/δ and Re_δ, the problem can be reposed as $C_f = C_f(k_s/x, Re_x)$ or $C_f = C_f(Re_k, Re_x)$, with $Re_x \equiv U_\delta x/\nu$ and $Re_k \equiv U_\delta k_s/\nu$. The additional relationship between x and δ is solved with the von Kármán momentum integral equation (for zero pressure gradient), $d\theta/dx = C_f/2$, where θ is the momentum thickness that can be calculated from the assumed profile (Equation 5). The procedure is readily tackled (Prandtl & Schlichting 1934, Granville 1958, Monty et al. 2016, Pullin et al. 2017). **Figure 3*b*** shows example drag curves resulting from this approach, highlighting a few subtle differences for this developing case. The curves at fixed Re_k assume that k_s is homogeneous over the length of the plate, showing the decrease of C_f toward the long-plate limit (large Re_x) of the smooth line (Pullin et al. 2017). The scenario yielding constant C_f in the developing boundary layer occurs in the fully rough regime when k_s/x is constant. This could occur where a fully rough k_s grows linearly along the plate (yielding a constant C_f along the entire length of the plate) (e.g., Sridhar et al. 2017). A more practical manifestation of this curve is for a fixed x location along a homogeneous fully rough plate, for which the constant k_s/x curves show that the C_f at this fixed location is not a function of the unit Reynolds number, U_δ/ν. For this scenario, δ would also be invariant with unit Reynolds number at a fixed x location (Pullin et al. 2017). Typically engineers are more interested in the integrated drag coefficient $\overline{C_f}$ ($= (1/L)\int_0^L C_f\,dx$) for a plate of length L, and for this reason these drag curves are often presented as $\overline{C_f}$ versus $Re_L \equiv U_\delta L/\nu$ (Granville 1958, Pullin et al. 2017).

For the cases with $k_s/\delta = 0.001$ in **Figure 3*a*** and with $k_s/x = 3 \times 10^{-7}$ and $Re_k = 3 \times 10^2$ in **Figure 3*b***, the three different line types show C_f resulting from different assumed behaviors of $B_s(k^+)$ in the transitionally rough regime: Colebrook, Nikuradse, and fully rough type. In the parameter space close to the smooth curve, uncertainty regarding the transitionally rough behavior can lead to errors in C_f that exceed 10%, and hence in this regime knowledge of k_s alone is insufficient to predict drag accurately. As an example of the importance of this regime, aircrafts have typical surface roughness of $k_s \approx 10$ μm (Moyes et al. 2017). In cruise conditions (altitude of 10 km, $U_\delta = 250$ m/s, $Re_k \approx 71$) and for a fuselage length of $L \approx 60$ m ($Re_L \approx 4.3 \times 10^8$, $k_s/L \approx 1.7 \times 10^{-7}$), the difference between the $\overline{C_f}$ for a Colebrook- or Nikuradse-type surface for

$k_s = 10$ μm is approximately 5%, highlighting the importance of understanding the roughness topographies that lead to these respective transitionally rough behaviors.

Frontal solidity: $\lambda_f \equiv A_f/A_t$, where A_f is the frontal projected area of roughness elements

Effective slope: $ES \equiv \frac{1}{A_t}\int \left|\frac{\partial h'}{\partial x}\right| \mathrm{d}A$, where h' is the variation in roughness elevation about the mean

Plan solidity: $\lambda_p \equiv A_p/A_t$, where A_p is the plan area of roughness elements

Skewness: $Sk \equiv \left(\frac{1}{A_t}\int h'^3 \,\mathrm{d}A\right)/k_{rms}^3$, where h' is the variation in roughness elevation about the mean and k_{rms} is the root-mean-square roughness height

Average roughness height: $k_a \equiv \frac{1}{A_t}\int |h'| \,\mathrm{d}A$, where h' is the variation in roughness elevation about the mean

Root-mean-square roughness height: $k_{rms} \equiv \sqrt{\frac{1}{A_t}\int h'^2 \,\mathrm{d}A}$, where h' is the variation in roughness elevation about the mean

***2N*-point-average peak-to-trough roughness height:** $k_z \equiv \frac{1}{N}\sum_{i=1}^{N}(k_{pi} + k_{vi})$, where $k_{pi} + k_{vi}$ is the ith-highest peak-to-trough height of the entire sample and $N = 5$ typically

Total plan area: A_t

3. RELATING SAND-GRAIN ROUGHNESS TO TOPOGRAPHY

The bottleneck in our ability to make full-scale predictions of drag (Section 2.3) is the lack of a proven method to ascribe k_s (Section 2.2.2) based solely on topographical features:

$$k_s = f(\text{measured topographical properties}). \qquad 6.$$

Thus, a great deal of research has been directed at attempts to correlate topographical features to k_s (for an extensive review, see Flack & Schultz 2010). A review of more recent attempts is given in Section 3.2. The ultimate challenge for research in this area is to produce a generalized model or correlation that is sufficiently robust to work across the range of rough surfaces that are encountered in applications. This challenge, as formulated in Equation 6, is essentially posing the question: Which topographical properties exert an influence on the flow and what is the bare-minimum set of these properties that would be required to estimate the drag of a surface? We address this question in Section 3.1.

3.1. Surface Properties

It is almost impossible to characterize roughness from the wide range of types, shapes, and surface morphologies. The first step is to adopt clearly defined and measurable surface parameters. What follows is an attempt to show that, as a bare minimum, a correlation between surface topography and wall drag is likely to require measures of (*a*) roughness height (k_a, k_{rms}, k_t, $\overline{k}_t$, or k_z); (*b*) frontal solidity λ_f, effective slope ES, or roughness density parameter Λ_s; and (*c*) plan solidity λ_p, skewness Sk, or solid volume fraction ϕ. Clustering and directionality are also important. This is not intended as an exhaustive list of the taxonomy of roughness, but rather as a set of parameters, with as little overlap as possible, that exert a known influence on the drag and hence the k_s of a surface. Limiting combinations of these topographical parameters and flow conditions may invalidate the desired formulation of Equation 6 (see Section 5).

3.1.1. Roughness height. As a first recourse, some measure of roughness height will be indispensable in relating a surface topography to k_s. Such measures include average roughness height k_a (e.g., Acharya et al. 1986), root-mean-square roughness height k_{rms} (the standard deviation of roughness elevation), or maximum peak-to-trough roughness height k_t. The former two, which involve area integrals, are less subject to corruption by extreme asperities and thus represent more reliable statistical measures of mean roughness amplitude. To partially circumvent these issues, one sometimes uses the subsample-average peak-to-trough roughness height $\overline{k}_t$, based on subareas of a surface (e.g., Thakkar et al. 2017) or sub-lengths of a surface, such as Rt_{50}, which is measured along 50-mm lines and commonly used in measuring ship hull roughness (Howell & Behrends 2006). Another option is k_z, the $2N$-point-average peak-to-trough roughness height, the average of the N highest peak-to-trough roughness heights over the entire sample (**Figure 1**), e.g., $N = 5$, the so-called ten-point height (Howell & Behrends 2006). However, alone, none of these properties is suitable for converting from topography to k_s, and other measures must be employed.

3.1.2. Frontal solidity. For an array of wall-mounted roughness elements (**Figure 4*a***), frontal solidity λ_f is simply the ratio of the projected frontal area, A_f, of roughness elements to the total plan area, A_t. Frontal solidity measures the available area exposed to pressure drag and can

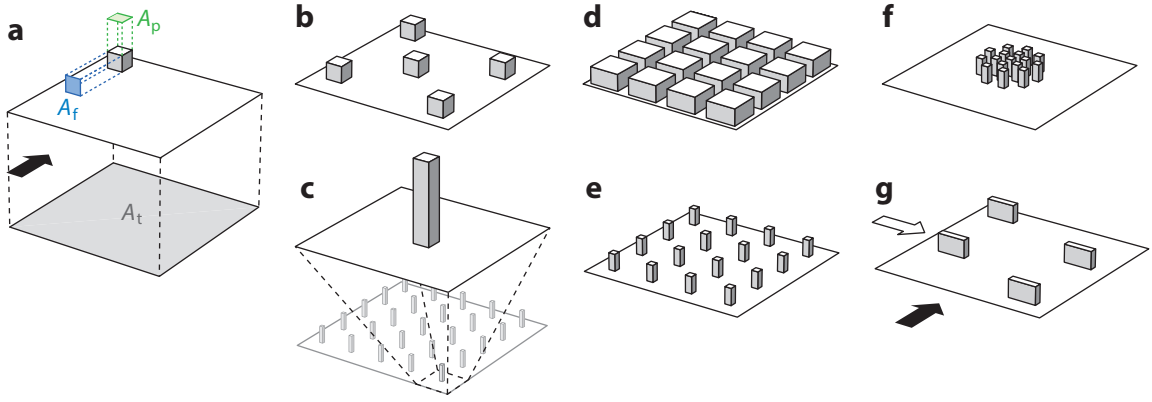

Figure 4

Surface sketches to illustrate frontal solidity (A_f) and plan solidity (A_p), as well as clustering and directionality. Open and filled arrows in panel *g* indicate different possible flow orientations.

imply a measure of density. Certainly the cube roughness illustrated in **Figure 4*b*** has a higher λ_f and denser packing than in **Figure 4*a***. Very sparsely packed or isolated roughness elements ($\lambda_f \to 0$, **Figure 4*a***) will tend toward smooth conditions since there will be increasing expanses of smooth-like conditions between elements, as will very densely packed roughness where individual elements will be sheltered due to proximity to neighbors (**Figure 4*d***). Between these regimes, there is typically a broad range, $0.1 \lesssim \lambda_f \lesssim 0.3$, where the drag ($k_s/k$, to be precise) is maximum (e.g., Schlichting 1937, Raupach et al. 1991, Jiménez 2004). Although a purely geometric characterization meant for the fully rough regime, the peak drag in the broad range $0.1 \lesssim \lambda_f \lesssim 0.3$ also appears to hold in the transitionally rough regime (MacDonald et al. 2016) (**Figure 5*a***). Though undoubtedly important, λ_f alone is inadequate. For example, the two very

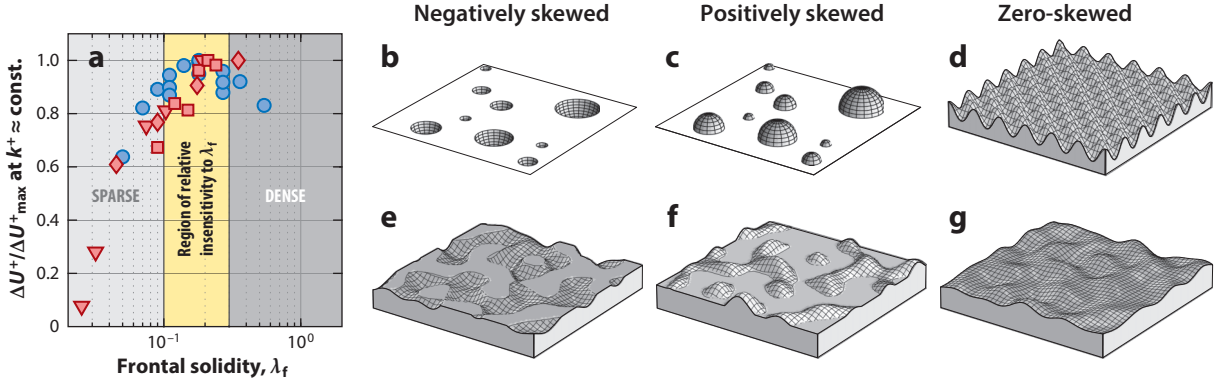

Figure 5

(*a*) The normalized roughness function, ΔU^+, presented as a function of frontal solidity, λ_f, for cases with fixed skewness, *Sk*: (*circles*) 3D sinusoids of Chan et al. (2015) and MacDonald et al. (2016) with $Sk = 0$ and a maximum peak-to-trough roughness height of $k_t^+ = 20$; (*diamonds*) fouled hydro turbine blade of Yuan & Piomelli (2014a) with $Sk = 0.135$ and an average roughness height of $k_a^+ = 67$; (*triangles*) 2D sinusoids of Napoli et al. (2008) with $Sk = 0$ and $k_a^+ = 19.75$; and (*squares*) block roughness of Placidi & Ganapathisubramani (2015) with $Sk = 1.05$ and $495 < k_t^+ < 615$. (*b–g*) Sketches of (*b*,*e*) negatively skewed, (*c*, *f*) positively skewed, (*d*) zero-skewness steep, and (*g*) zero-skewness shallow surfaces. The irregular surfaces in panels *e–g* are adapted from Jelly & Busse (2018), and the zero-mean elevation variation h' of panel *g* was reduced to maintain matched λ_f.

different packing densities and element aspect ratios illustrated in **Figure 4*b*,*c*** have the same λ_f and height. The plan solidity λ_p (Section 3.1.3) is needed to distinguish between these cases.

3.1.2.1. Effective slope. The mean absolute streamwise gradient of a rough surface is known as the effective slope, *ES* (Musker 1980, Napoli et al. 2008). This measure is equivalent to twice the frontal solidity, $\lambda_f = ES/2$ (Thakkar et al. 2017), so in some sense it adds little to our ability to parametrize surfaces. However, it illustrates the point that low λ_f can be thought of as either sparsely packed (**Figure 4*b***) or long-wavelength shallow roughness (**Figure 5*g***). Likewise, high λ_f could be considered as either densely packed (**Figure 4*d***) or short-wavelength steep roughness (**Figure 5*d***). In distinguishing between shallow and sparsely packed topographies, it is necessary to introduce a measure of skewness (Section 3.1.3). As an example, the shallow surface shown in **Figure 5*g*** has the same *ES* as the cases illustrated in **Figure 5*e*,*f***, the difference being that these cases have zero, negative, and positive skewness, respectively. In the transitionally rough regime, the irregular surfaces of Flack et al. (2019) (at fixed $Sk \approx 0$) show that low-*ES* surfaces approach Colebrook behavior, while high-*ES* surfaces approach Nikuradse behavior.

3.1.2.2. Roughness density parameter. The parameter $\Lambda_s = \lambda_f^{-1}(A_f/A_w)$, where A_w is the total windward wetted surface area, has been suggested by Sigal & Danberg (1990) and van Rij et al. (2002). Bons (2005) showed that the local value of Λ_s is related to the local angle $\alpha_h = \arctan(\partial b'/\partial x)$ for small α_h. Since $|\alpha_h|$ is approximately $ES \propto \lambda_f$ locally, a strong relationship between all four measures may be expected globally, as evidenced by Thakkar et al. (2017), who have suggested that only one is sufficient for correlations.

3.1.3. Plan solidity. When combined with λ_f, plan solidity λ_p, defined as the ratio of the plan area, A_p, of roughness elements to the total plan area, A_t (**Figure 4*a***), can give an improved measure of the roughness form. Indeed, models (Macdonald et al. 1998, Grimmond & Oke 1999) predict that the λ_f at which the drag is maximum depends on λ_p (see **Figure 6*a*** and Placidi & Ganapathisubramani 2015). High plan solidities ($\lambda_p \to 1$) suggest densely packed arrangements (**Figure 4*d***). Such surfaces tend to be negatively skewed (Section 3.1.3). Cases with $\lambda_p \to 0$ imply sparsely packed arrangements with a resulting positive skewness. The ratio of λ_f/λ_p can, in some scenarios, give an indication of the aspect ratio of the roughness elements. For example, a cube-like element will have $\lambda_f/\lambda_p = 1$ (**Figure 4*b***), a squat element will have $\lambda_f/\lambda_p < 1$ (**Figure 4*d***), and tall thin elements will have $\lambda_f/\lambda_p > 1$ (**Figure 4*c*,*e***). Such generalizations can be corrupted in situations where elements are clustered (Section 3.1.4).

3.1.3.1. Skewness. A measure of the asymmetry in surface-elevation distribution is skewness, *Sk*. In general, pitted surfaces will be negatively skewed (**Figure 5*b*,*e***) and surface deposits will be positively skewed (**Figure 5*c*,*f***) [see Monty et al. (2016), included here in **Figure 2*b*,*c***, for a practical example of a highly positively skewed surface ($Sk \approx 3.0$)]. For wall-mounted cubes (**Figure 4*b***), a measure of skewness is conveyed by the plan solidity λ_p, where $\lambda_p > 0.5$ implies $Sk < 0$ and vice versa, as $Sk = (1 - 2\lambda_p)/[\lambda_p(1 - \lambda_p)]^{1/2}$, the one-to-one correspondence demonstrating that they contain the same information. However, this relationship does not hold in general [e.g., for pyramids, with $\lambda_p = 1$ but $Sk > 0$ (Schultz & Flack 2009)]. Unlike λ_p, *Sk* is easily calculated for irregular surfaces, and the floor on which elements are mounted need not be defined. From a study of replicated ship hull roughness, Musker (1980) suggested that *Sk* (along with *ES* and k_{rms}) is critical in relating topography to k_s, as corroborated by a growing number of systematic studies (Flack & Schultz 2010, Jelly & Busse 2018, Flack et al. 2019). Specifically, Jelly & Busse (2018) have shown that, for two irregular surfaces with matched k_a^+ and $ES = 0.17$,

the peaked surface ($Sk \approx 1.62$) produces much more drag than the pitted surface ($Sk \approx -1.64$). This is consistent with the irregular surfaces investigated by Kuwata & Kawaguchi (2019), with $ES \approx 0.31$–0.52, and also with the irregular surfaces investigated by Flack et al. (2019), where five surfaces with matched $ES \approx 0.37$ showed k_s/k_{rms} increasing with Sk. In terms of transitionally rough behavior, the most positively skewed of these five surfaces ($Sk \approx 0.84$) showed abrupt transition from hydraulically smooth to transitionally rough behavior at large $k_s^+ \approx 10$, echoing an earlier finding of Monty et al. (2016) (**Figure 2*b*,*c***).

3.1.3.2. Solid volume fraction. Common in the canopy literature (Nepf 2012), the solid volume fraction, ϕ, occupied by roughness between the maximum and minimum roughness elevation can be viewed as a volume-based generalization of the area-based λ_p. Formally, it is also given by $\phi = [\overline{h} - \min(h)]/[\max(h) - \min(h)]$ and ranges between 0 and 1. If ϕ is small, $\overline{h}$ would approach $\min(h)$, whence $h' \equiv h - \overline{h}$ would tend to be positive and thus $Sk > 0$. Although strictly unequal, ϕ, λ_p, and Sk characterize related topographical features.

3.1.4. Parameters characterizing arrangement. In this section we look at topographical properties that are known to be important but lack well-accepted metrics.

3.1.4.1. Clustering. Roughness height, skewness, and frontal and plan solidity fail to capture clustering or spatial homogeneity. The examples shown in **Figure 4*e*,*f*** all have the same k_a, Sk, λ_f, λ_p, and all higher-order moments (due to their identical elevation distributions), yet the 16 elements per unit plan area are arranged in very different manners, with different expected outcomes on the flow. Sarakinos & Busse (2019) tested surfaces with matched topographical properties, but varying degrees of clustering, noting that ΔU^+ decreases with increased clustering. Clustering, related to heterogeneity (Section 5.2), can appear as a spatial modulation of the roughness elevation. Hence, spatial correlations or spectra of surface elevation can fail to adequately characterize the effect of clustering. Not strictly related to clustering, but in some sense associated with small-scale heterogeneity, Forooghi et al. (2017) compared surfaces with matched topographical properties but varying degrees of height polydispersity (measured by the range relative to the mean), finding that for surfaces with matched k_{rms}, regularly sized (monodisperse) roughness elements lead to a larger k_s than disparately sized (polydisperse) roughness elements.

3.1.4.2. Directionality. The concept of directionality, or anisotropy, is due to either shape or alignment of roughness elements. **Figure 4*f*,*g*** offers a comparison between two surfaces with the same k_a, Sk, λ_f, and λ_p, yet with different levels of directionality. The roughness shown in **Figure 4*f*** is isotropic in the sense that the drag would be relatively invariant with flow direction, whereas the anisotropic roughness shown in **Figure 4*g*** has aligned features, where we may expect the pressure drag (and λ_f; Section 3.1.2) to be very different if the flow were from the direction of the open or closed arrow. Indeed, Busse & Jelly (2020) show that spanwise-aligned surface patterns tend to have a higher drag penalty than streamwise-aligned surface patterns, as the spanwise-aligned surface patterns considered feature higher $\lambda_f = ES/2$. Regularity is bound up with notions of directionality: A regular surface is often anisotropic. Forooghi et al. (2017) compared three surfaces with matched k_{rms}^+, ES, and Sk, but where the roughness elements were arranged randomly or regularly in staggered or streamwise-aligned arrangements. All three cases have differing degrees of anisotropy, but, in this example, they have matched $\lambda_f = ES/2$ (in contrast to the two flow directions shown in **Figure 4*g***), with the streamwise-aligned arrangement producing the lowest ΔU^+. Another observation highlighting the effect of arrangement is that due to Yuan & Piomelli (2014a), who noted that irregular surfaces (at fixed $k_{rms}^+ \approx 25$ and $Sk \approx 0.135$) attain a maximum

ΔU^+ at higher ES ($\approx$0.7) than regular surfaces, e.g., 3D sinusoids (at fixed $k^+_{rms} = 5$ and $Sk = 0$) (MacDonald et al. 2016), where the maximum ΔU^+ occurs at $\lambda_f = ES/2 \approx 0.15$ (**Figure 5*a***). Thakkar et al. (2017) considered the transitionally rough regime of 17 industrial surfaces, finding that ΔU^+ could be best predicted from a correlation based on λ_f, Sk, and k_{rms}, as well as the ratio of streamwise correlation length to k_t, the latter representing an addition to the bare-minimum set (Section 3). A measure of directionality is the surface texture aspect ratio S_{tr} (Thakkar et al. 2017, Busse & Jelly 2020), the ratio of the shortest correlation length of all directions to the longest correlation length of all directions. Surfaces with $S_{tr} < 0.3$ (0 for all 2D roughnesses) are considered directional, while surfaces with $S_{tr} > 0.5$ are considered isotropic.

Highly directional surfaces can lead to atypical drag behaviors. For example, riblets ($S_{tr} = 0$), when flow aligned, feature a distinct narrow range of small sizes k^+ with $\Delta U^+ < 0$, indicating that drag is reduced below smooth-wall levels (Bechert et al. 1997, García-Mayoral et al. 2019). Not only that, but in the drag-increasing regime of large k^+, riblets fail to conform to the fully rough asymptote (Gatti et al. 2020). In some sense this is not surprising, since the fully rough asymptote is associated with the dominance of pressure drag over viscous drag, which cannot be the case with flow-aligned riblets that have no surface normals with a streamwise component on which pressure drag can act. It is also conceivable that larger-scale directional surfaces could selectively interact with or bias turbulence at particular scales and subsequently violate outer-layer similarity, e.g., the streamwise-aligned 3D roughness arrangement of Forooghi et al. (2017) and the drag-increasing riblets (large k^+) of Newton et al. (2018), the latter showing that the turbulence structure, even far from the wall, is profoundly altered.

3.2. Predictive Correlations

In the fully rough regime, Equation 6 can be formulated, at a bare minimum (Section 3.1), with k_s/k as a function of a slope parameter (e.g., λ_f, ES) and a skewness parameter (e.g., λ_p, Sk). **Figure 6**

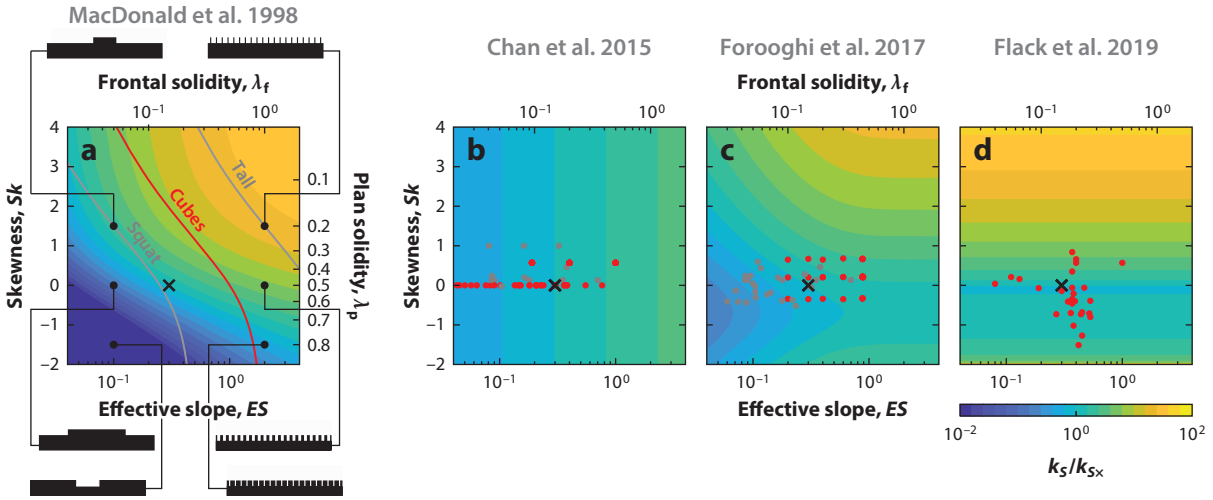

Figure 6

Contours of equivalent sand-grain roughness height, k_s, according to predictive correlations in the fully rough regime. Each correlation is normalized by $k_{s\times}$, the respective k_s value at a frontal solidity of $\lambda_f = 0.15$ or effective slope of $ES = 0.3$ and a plan solidity of $\lambda_p = 0.5$ or skewness of $Sk = 0$ (indicated by $\times$): (*red circles*) fitting data and (*gray circles*) additional test data. The red $\lambda_f = \lambda_p$ line (cube roughness) in panel *a* indicates the fitting data; the gray lines show $\lambda_f = \lambda_p/4$ (squat elements) and $\lambda_f = 5\lambda_p$ (tall elements).

presents four predictive correlations for k_s/k. Since these correlations each use different measures for k (k_t, k_a, $\overline{k}_t$, k_{rms}), all panels in **Figure 6** are normalized by their respective values for k_s at the common location $ES = 0.3$ and $Sk = 0$, denoted by $k_{s\times}$. The data on which the correlations were developed are also represented in **Figure 6**, all of which are near the reference $k_s/k_{s\times} = 1$ location, except for **Figure 6*a***, which is based on cube data along the line $\lambda_f = \lambda_p$.

Figure 6*d* shows the correlation of Flack et al. (2019), based on Flack & Schultz (2010),

$$k_s = 2.48\,k_{rms}(1 + Sk)^{2.24}, \quad k_s = 2.11\,k_{rms}, \quad \text{and} \quad k_s = 2.73\,k_{rms}(2 + Sk)^{-0.45}, \tag{7.}$$

for $Sk > 0$, $Sk = 0$, and $Sk < 0$ surfaces, respectively. Equation 7 was developed using a wide range of roughness topographies, from gravel (Castro 2007) to commercial steel pipe (Shockling et al. 2006), but it includes no measure of ES (suggested as a bare-minimum set in Section 3.1). Equation 7 was predominantly formulated for surfaces that have a relatively narrow range of ES in which k_s/k is relatively invariant (Jiménez 2004) (cf. **Figure 5*a***), avoiding sparse or dense surfaces. Barros et al. (2018) have shown that Equation 7 can be extended to lower-ES surfaces if long-wavelength contributions are filtered out prior to computing statistics. Forooghi et al. (2017) studied 38 surfaces with both regular and irregular arrangements and size distributions of roughness elements of prescribed shape and proposed, for polydisperse roughness,

$$k_s = \overline{k}_t(0.67\,Sk^2 + 0.93\,Sk + 1.3)[1.07(1 - e^{-3.5\,ES})], \tag{8.}$$

shown in **Figure 6*c***, which has all the ingredients suggested in Section 3.1. A slightly different correlation is available for roughness with nearly uniform size distributions (i.e., monodisperse roughness). Chan et al. (2015) studied 3D sinusoidal roughness, systematically investigating the influence of roughness height and wavelength. They showed that ΔU^+, in the transitional and fully rough regimes, depends on both k_a^+ and ES, proposing

$$k_s \approx 7.3\,k_a\,ES^{0.45}, \tag{9.}$$

shown in **Figure 6*b***. Equation 9 was formulated together with a data compilation covering a wide range in ES, but narrow in Sk, explaining the omission of the latter parameter. **Figure 6*a*** shows the correlation of Macdonald et al. (1998), given as

$$k_s \approx 30k_t(1 - d/k_t)\exp\left\{-[0.5(1.2/0.4^2)(1 - d/k_t)\lambda_f]^{-0.5}\right\}, \tag{10.}$$

with $d/k_t = 1 + 4.43^{-\lambda_p}(\lambda_p - 1)$. Equation 10 was based on a physical model with the constants here tuned for staggered cube roughness (the cube case is represented by the $\lambda_f = \lambda_p$ line in **Figure 6**).

In general, a graphical comparison of these four correlations indicates that each is formulated from data that cover a relatively narrow region of the parameter space. Use of these correlations beyond these respective regions involves a dangerous degree of extrapolation. Even so, there are some common characteristics. **Figure 6*a–c*** all show monotonically increasing k_s/k with increasing ES. As such, these three correlations only seem to be applicable to the sparse λ_f regime, despite being formulated on data that includes dense surfaces, as in **Figure 6*a*,*b***. At fixed Sk, data (Placidi & Ganapathisubramani 2015, MacDonald et al. 2018) suggest that k_s/k will increase with ES for $ES \lesssim 0.3$–0.6, beyond which it will eventually decrease in the dense fully rough regime, $ES \gtrsim 0.4$–3, depending on the roughness topography. None of the correlations shown here captures this constant-Sk or constant-λ_p behavior, perhaps because the decrease of k_s/k with increasing ES at constant Sk has not been seen for irregular surfaces up to $ES \approx 0.8$–0.9 (e.g., Yuan & Piomelli 2014a, Forooghi et al. 2017). However, a peak is predicted by the model of **Figure 6*a*** along $\lambda_p = \lambda_f$ (cf. Placidi & Ganapathisubramani 2015). Along $\lambda_p \propto \lambda_f$ intersects, **Figure 6*a*** shows a differing λ_f location of k_s/k peaks, depending on whether the elements are squat or tall. There

are also commonalities in terms of skewness. In the positively skewed regime, **Figure 6*a*,*c*,*d*** all show increasing k_s/k with increasing Sk (draggy peaks), with both panels *c* and *d* further indicating minima in k_s/k with Sk occurring at $Sk \approx -1$ and 0, respectively. Interestingly, panels *a* and *c* both show diagonal contours around the reference $k_s/k_{s\times} = 1$ location, perhaps demonstrating the robustness of the physics-constrained fit (**Figure 6*a***) away from the fitting data.

An all-encompassing equation relating k_s to topography remains elusive. In many respects, progress in this endeavor is linked to an improved appreciation of key topographical parameters and will be aided by systematic studies that painstakingly isolate the effect of certain topographical features (i.e., sweeps through the parameter space in **Figure 6**). Coles's (1968) view on the usefulness of varying only one parameter at a time remains pertinent. In understanding the wider picture of topographical effects, it would also be useful to populate the extremities of the parameter space in **Figure 6** where there is currently a dearth of systematic data. Readers are encouraged to use and contribute to a recently developed roughness database (**http://roughnessdatabase.org/**) that contains surface profiles and statistics, as well as experimental measurements or simulation results for flow over a wide range of roughness topographies.

4. ADVANCES IN EXPERIMENTS AND COMPUTATIONS

In the past, a trial-and-error approach was, by necessity, adopted to investigate the effect of largely random variations in roughness topography. For this reason, identifying key roughness parameters and quantifying their influence have been troublesome, but recent advances in experiments and computations have been lowering the barriers.

4.1. Experiments

Experimental investigations have been aided by the commissioning of several high–Reynolds number pipe (Shockling et al. 2006), channel (Barros et al. 2018), and boundary-layer (Squire et al. 2016) flow facilities. Further advances focus on the accurate measurement of wall shear stress, which has long hindered experimental studies. The limitations of the Clauser chart (Perry & Joubert 1963) are well documented (Castro 2007). While direct measurement using floating-element balances is not new (Acharya et al. 1986), the last decade has seen widespread adoption of this technique for studying roughness (Krogstad & Efros 2010, Placidi & Ganapathisubramani 2015, Squire et al. 2016). Taylor–Couette flow can potentially be exploited, as the wall shear stress can be accurately determined from torque (Zhu et al. 2018). The roughness function measured in Taylor–Couette flow is similar to that of pipe flow, but whether both flows yield the same k_s independent of radius ratio remains to be resolved (Berghout et al. 2019). Volino & Schultz (2018) proposed an indirect method for determining wall shear stress based on the streamwise momentum equation, later expanded by Womack et al. (2019). An increasing availability of rapid prototyping and CNC (computer numerical control) capabilities now permits test surfaces to be readily manufactured from surface scans and mathematically generated topographies (Johnson & Christensen 2009, Schultz & Flack 2009, Flack et al. 2019), which has in turn led to more systematic experimental studies of key topographical parameters.

4.2. Computations

Roughness-resolving direct numerical simulation (DNS) is now routine, thanks to increases in hardware performance and to the maturing of the immersed-boundary method (Fadlun et al. 2000) for representing complex boundaries in efficient solvers. The immersed-boundary

method, which simplifies the otherwise cumbersome meshing of roughness boundaries, has been used to study flow over regular roughness (e.g., Leonardi et al. 2003) and irregular roughness, synthesized (e.g., Yuan & Piomelli 2014b) or scanned (e.g., Thakkar et al. 2018). A newcomer that also promises a simple representation of complex boundaries is the lattice Boltzmann method (e.g., Kuwata & Kawaguchi 2019). Body-fitted meshes remain tenable for regular topographies (e.g., Coceal et al. 2007) due to the simpler meshes and repeating features. A point to consider is the higher cost, relative to smooth walls, of resolving small features when viscous drag dominates. Irregular surfaces, for example, require $\gtrsim$12 points per smallest feature (Busse et al. 2015), which increases the cost of studying the transitionally rough regime in the smooth-wall limit (Thakkar et al. 2018). If the primary goal is to characterize the drag penalty of small-scale roughness, the low-cost minimal-channel DNS could be employed to directly simulate the roughness sublayer without resolving the outer flow (Chung et al. 2015, MacDonald et al. 2017), i.e., the physical basis for this method is Townsend's outer-layer similarity (Section 2.1). Another cost-saving approach is to partially resolve the roughness topography while performing LES with coarser meshes away from the wall (e.g., Napoli et al. 2008, Yuan & Piomelli 2014a, Nikora et al. 2019). LES with wall-modeled roughness (e.g., Anderson et al. 2015, Sridhar et al. 2017), i.e., imposing the local shear stress according to a log law with prescribed roughness length y_0, allows for spatial variations of roughness properties at the level of the LES mesh spacing, and is suited for studying heterogeneous roughness. For multiscale roughness, an innovation is the dynamic scale-similarity closure for prescribing y_0 from surface-elevation distributions (Anderson & Meneveau 2011). Also possible is LES with immersed boundaries to resolve the larger roughness elements (presumably contributing the most to drag) while wall-modeling the unresolved roughness (Yang et al. 2016).

5. LIMITING ROUGHNESS TYPES

While a large number of roughnesses, given k_s (Section 3), behave according to the framework of Section 2, there are subtleties that require care or situations where the framework fails, sometimes expectedly, but also sometimes unexpectedly. Here we try to discuss the known odd (and fascinating) behaviors, grouping them into dense, nonhomogeneous, multiscale, and wavy roughness. These groups are neither mutually exclusive, e.g., multiscale roughness can also be nonhomogeneous, nor exhaustive, representing only a selection to highlight the rich flow physics encountered in the study of roughness. It is, however, essential that roughness practitioners, where possible, develop an eye for surfaces that will lead to atypical behaviors, since these will necessitate different approaches.

5.1. Dense Roughness

When the roughness topography becomes denser at a given height k, exceeding $\lambda_f \gtrsim 0.15$, it is well known (e.g., Jiménez 2004) that the roughness becomes less draggy, that is, k_s/k (or ΔU^+ at fixed k^+) decreases with increasing λ_f (cf. **Figure 5*a***). Further increasing λ_f at fixed k^+ ultimately narrows the fluid gap between roughness elements down to the viscous scale ν/u_τ, where a gap-based Reynolds number takes precedence over geometric parameters and k^+ in describing the flow. In the extreme, e.g., sinusoidal wavelength $\lambda^+ \lesssim 3$ (MacDonald et al. 2016) and interblock fluid gap $\mathcal{W}^+ \lesssim 2$ (Sharma & García-Mayoral 2020), the flow approaches that of a smooth wall at the roughness crest. For $\lambda_f \gtrsim 0.15$, the flow is thought to skim over the roughness (e.g., Grimmond & Oke 1999), but if the roughness is dense ($\lambda_f \gg 0.15$), the skimming flow no longer reaches the base of the roughness elements. The transverse square $k \times k$ bars (i.e., $\lambda_f = \lambda_p$) with varying fluid

gap $\mathcal{W}$ come to mind. For approximately fixed k^+, ΔU^+ increases for $\lambda_f = 0.017$–0.1 and then decreases for $\lambda_f = 0.25$–0.5, consistent with the $\lambda_f \approx 0.15$ peak (Leonardi et al. 2007), but at fixed $\lambda_f = 0.5$, ΔU^+ appears insensitive to k^+ up to $k^+ \approx 80$, and at $\lambda_f = 0.67$, trapped mean vortices in the gaps no longer reach down to the base. However, in a study of deep transverse bars of depth k, thickness b, and fluid gap $\mathcal{W} = b$ (i.e., fixed $\lambda_p = 0.5$), MacDonald et al. (2018) suggested that even extremely dense surfaces, $\lambda_f > 0.5$, eventually exhibit fully rough behavior (at fixed λ_f). Their $\lambda_f = 1.5$ data are included in **Figure 2*b*,*c***, showing that the fully rough asymptote of ΔU^+ is approached at sufficiently high k^+. Once the bars are deep enough ($\lambda_f \geq 1.5 \gg 0.15$), the relevant parameter for collapsing ΔU^+ is $\mathcal{W}^+$, i.e., $\Delta U^+ \sim (1/\kappa)\ln \mathcal{W}^+ + \text{constant}$, independent of k^+ (equivalently, $k_s \propto \mathcal{W}$ or $k_s/k \propto \lambda_f^{-1}$) (MacDonald et al. 2018). This is because the flow is stagnant deep in the gap and the turbulent flow around and above the crest only sees the fluid gap $\mathcal{W}$ and not the depth k. In addition to 2D transverse bars, 3D block arrays also show a similar importance of the fluid gap over the roughness height in the dense regime (Sharma & García-Mayoral 2020), where ΔU^+ saturates with k^+ beyond $\lambda_f \gtrsim 2.0$ at fixed $\lambda_p = 0.25$.

Dense roughness topographies ($\lambda_f \gg 0.15$) arise naturally in the study of canopies, where similar concepts have been studied in depth (Finnigan 2000, Nepf 2012). The customary geometrical parameter is not the canopy height, k, but a^{-1}, which is related to the lateral spacing of obstructions, defined as the frontal area per unit volume, i.e., $a \equiv A_f/(kA_t) = \lambda_f/k$, such that $\lambda_f = ka$. Additionally, the solid volume fraction, ϕ, is related to the plan density, λ_p. The sparse–dense delineation at $ka \approx 0.1$ (cf. $\lambda_f \approx 0.15$) is well known for canopies (Nepf 2012). The idea that drag concentrates near dense canopy tops such that the canopy height becomes dynamically irrelevant (Nepf 2012) is also evidenced in deep bars (MacDonald et al. 2018), where the force centroids become independent of k^+ for $\lambda_f \geq 1.5 \gg 0.15$. It is customary to parametrize the canopy drag (per unit volume) $D(y)$ as $D \equiv (1/2)(C_D a)\rho U^2$, where the drag length $(C_D a)^{-1}$ is a hydraulic length that plays the same role to the geometric spacing a^{-1} as that of k_s to k. Because hydraulic lengths, by construction, relate to drag, k_s and $(C_D a)^{-1}$ are connected. For dense canopies, momentum is fully absorbed at penetration depth $\propto \epsilon \approx k - d \ll k$ below the canopy top such that the wall shear stress τ_w is approximately equal to $\int_d^k D\,\mathrm{d}y \approx D(k)\epsilon$ or, in parametrized form, $(1/2)(C_D a)\epsilon[U^+(k)]^2 \approx 1$. Then, using the fully rough log law evaluated at the crest, $U^+(k) \approx (1/\kappa)\ln(\epsilon/k_s) + B_s(\infty)$, and noting $(C_D a)\epsilon \approx 0.23$ (Luhar et al. 2008, Nepf 2012), we obtain $k_s \approx 2.1(C_D a)^{-1}$. In the dense regime, this relationship suggests $y_0/k \propto k_s/k \propto (C_D a k)^{-1} \propto \lambda_f^{-1}$. These links were already noted earlier, including counterparts in the sparse and transitionally rough regimes (Raupach 1994, Luhar et al. 2008, Nepf 2012). A similar idea is used in the study of porous surfaces, where a hydraulic permeability length scale $\sqrt{K}$, proportional to the pore size, is the relevant parameter, as opposed to the porous-bed thickness (Breugem & Boersma 2005, Voermans et al. 2017).

For deep roughness topographies such as porous surfaces in pressure-driven flows, u_τ, which scales the turbulence above, need not be related to the total drag on the roughness elements because not all of the momentum absorbed originates from the turbulence above the roughness crest (Breugem et al. 2006, Pokrajac et al. 2006) (which complicates, among other things, the assessment of outer-layer similarity from u_τ, as determined from either wall drag or pressure drop). Some of the momentum absorbed comes from interstitial fluid motion driven by the pressure gradient. Extrapolations of the linear total stress profile to the wall offset (Chan-Braun et al. 2011, García-Mayoral et al. 2019) or to the crest (Pokrajac et al. 2006, MacDonald et al. 2018) have been proposed as ways to determine u_τ, the former more physical, the latter more convenient. A further issue is the ambiguity of the drag for 2D transverse roughness in a closed geometry where the cross-sectional area changes with streamwise location (MacDonald et al. 2018).

5.2. Nonhomogeneous Roughness

The engineering tools that we have for predicting wall-bounded turbulent flows over rough surfaces all assume a homogeneous distribution of roughness. Yet, in applications, roughness is invariably patchy or heterogeneous. For the purposes of this review, a heterogeneous or nonhomogeneous roughness is defined as one in which the statistical properties of the roughness vary over a scale that is large relative to the outer scale, δ (e.g., boundary-layer thickness), of the flow. Examples include patchiness of biofouling on ship hulls, crop and forest boundaries in atmospheric surface layers, and rivet rows and panel joints on aircraft fuselages. In all of these instances, the overarching objective is to predict the adjustment of drag over these surfaces. Faced with the infinite possibilities of heterogeneous arrangements, researchers have focused on simplified kernel distributions to unpack the problem.

5.2.1. Streamwise variation in roughness. The smooth-to-rough and rough-to-smooth transitions in the streamwise direction have long been an important test case (Antonia & Luxton 1971, 1972). In these cases, the sudden change to a new surface condition generates an internal boundary layer, of thickness $\delta_i(x)$ (Elliot 1958), that demarcates a near-wall layer, which feels the new surface condition, from the flow farther from the wall, which retains a memory of upstream surface conditions prior to the surface transition. Though a useful modeling construct, the internal layer is not well defined, with a multitude of differing definitions (Rouhi et al. 2019). In the rough-to-smooth transition, the local wall shear stress C_f undershoots the equilibrium (homogeneous) smooth-wall value immediately downstream of the transition, taking several δ in fetch to recover (e.g., Antonia & Luxton 1972, Hanson & Ganapathisubramani 2016, Ismail et al. 2018, Li et al. 2019). A collation (Li et al. 2019) of local C_f recoveries reported from experimental and computational studies of a rough-to-smooth transition indicates that the scatter in integrated drag over the first 10δ downstream of transition differs by up to 40% between studies, suggesting a pressing need to better predict this flow. One modeling challenge is that the near-wall flow, even very close to the surface, requires a substantial fetch to recover equilibrium conditions, giving rise to the concept of the internal equilibrium sublayer with thickness $\delta_e \ll \delta_i$ (cf. Brutsaert 1982, Garratt 1990), within which similarity of the mean profiles with the local τ_w is observed. Recovery distances in excess of 10δ have been suggested before profiles start to exhibit local equilibrium (Ismail et al. 2018, Li et al. 2019).

These studies of streamwise variation in roughness also raise questions regarding the development of external turbulent boundary layers. In such cases, even with a homogeneous distribution of k_s, the dimensionless roughness scale k_s^+ (and k_s/δ) will vary in the streamwise direction. In such situations one might expect a continual progression of weak internal layers, such that at a given x location, the outer parts of the flow will retain a memory of the roughness condition from some distance $\mathcal{O}(20\delta)$ upstream. These effects will be more pronounced where the flow is subject to aggressive changes in x, arising even in zero-pressure-gradient flows at low δ^+ (Squire et al. 2016), possibly delaying recovery to outer-layer similarity of the turbulence.

5.2.2. Spanwise variation in roughness. In this case, roughness-induced turbulence anisotropy and spanwise gradients in turbulent stresses lead to the formation of Prandtl's secondary flows of the second kind (Hinze 1967, Anderson et al. 2015). Long a concern in hydrological flows over bed roughness (e.g., Colombini & Parker 1995), spanwise heterogeneity has seen a recent revival in interest in the engineering community following a study by Mejia-Alvarez & Christensen (2013), who observed stationary large-scale features in the turbulent boundary layer formed over a replicated fouled turbine blade. There has since been a slew of studies that have

looked at idealized spanwise heterogeneity, typically consisting of spanwise-alternating rough and smooth strips of some form. These studies show that the sense and strength of the secondary flows are sensitive to spanwise variations in both the roughness length y_0 (strip type; Anderson et al. 2015, Chung et al. 2018) and the wall offset d (ridge type; Hwang & Lee 2018), as envisioned by Colombini & Parker (1995), the complication being that many spanwise heterogeneous surfaces are a combination of these two effects (Vanderwel & Ganapathisubramani 2015, Medjnoun et al. 2018, Yang & Anderson 2018). Surfaces that lie between pure strip and pure ridge type can lead to either upward or downward flow over the regions considered to be roughest (Stroh et al. 2020). More complicated scenarios can arise where there are additional length scales, e.g., a difference in strip widths (Yang & Anderson 2018), broadband heterogeneity (Mejia-Alvarez & Christensen 2013), and directionality (Nugroho et al. 2013).

For strip-type roughness, the diameter, strength, and arrangement of secondary flows is strongly dependent on the repeating spanwise wavelength, Λ, relative to the outer scale, δ. In general, in the case of large Λ ($\gg\delta$), the secondary flows (of diameter $\approx\delta$) will be isolated, located at the lateral transition in surface conditions. Away from the location of secondary flows, the local surface conditions will dominate: slower flow over rougher patches and faster flow over smoother patches with outer-layer similarity observed based on the local wall drag (Chung et al. 2018, Wangsawijaya et al. 2020). As Λ reduces (to $\approx 2\delta$), the secondary flows (still of diameter δ) become space filling, forming counter-rotating pairs in the mean. Importantly, this wavelength seems to approximately coincide with the maximum strength of the secondary flows and also the maximum wall drag (Chung et al. 2018, Medjnoun et al. 2018, Yang & Anderson 2018, Wangsawijaya et al. 2020). As Λ reduces still further, the secondary flows (which have diameter $\approx\Lambda/2$ for $\Lambda \lesssim 2\delta$) weaken and are increasingly constrained closer to the surface. As the homogeneous limit is approached, $\Lambda \ll \delta$, we see a return to outer-layer similarity based on an averaged wall drag condition, with spanwise homogeneity observed for $y \gtrsim \Lambda/2$. Identifying Λ as the wavelength of the largest spanwise feature, this same limit ($y_r \approx 0.5\Lambda$) coincides with the height of the roughness sublayer ($y_r \approx 0.5\lambda$) over homogeneous roughness (Chan et al. 2018). Hence the roughness sublayer can be viewed as a measure of spanwise heterogeneity, or the wall-normal extent of the secondary flows.

5.3. Multiscale Roughness

In practice, many rough surfaces are irregular with a broad distribution of scales. Studies on filtering and low-order representations of multiscale roughness seek to account for flow behavior according to surface scales. For example, Johnson & Christensen (2009) and Mejia-Alvarez & Christensen (2010) tested the flow response of low-order representations (containing the first few singular value decomposition basis functions) of the turbine blade roughness of Bons et al. (2001), while Busse et al. (2015) tested surfaces obtained by progressively filtering a scanned graphite surface, varying the cutoff filter wavelength from $\approx 0.66\delta$ to $\approx 30\nu/u_\tau$. As more and more small scales are omitted, ΔU^+ decreases, which is perhaps not surprising due to the reduced k^+_{rms}, but it is also likely due to the reduced *ES*. This conclusion echoes that of Barros et al. (2018), who investigated the fractal surfaces of Anderson & Meneveau (2011), and that of Stewart et al. (2019), who also looked at fractal surfaces. Surfaces with the weakest small-scale surface-elevation variations (strongest spectral decay at high wavenumbers) exhibited the lowest drag. Physically, this means that long, shallow surface features are less draggy than short, steep surface features, consistent with the *ES* of the surfaces. Nikora et al. (2019) reported an interdependence between temporal velocity fluctuations and spatial variations of the time-averaged velocity (Nikora et al. 2007), a kind of scale interaction, over the fractal surfaces of Stewart et al. (2019), with results similar to

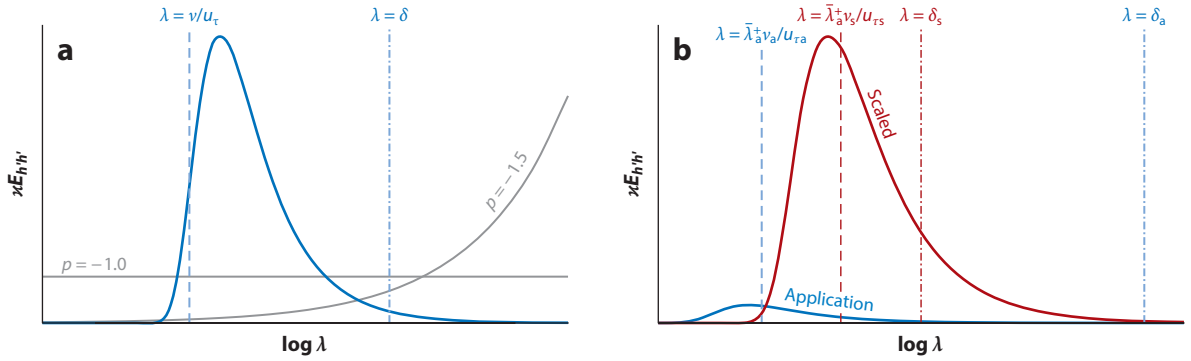

Figure 7

(*a*) Examples of premultiplied surface-elevation spectra, $\varkappa E_{b'b'}$, where $\varkappa$ is an in-plane wavenumber and $\lambda \equiv 2\pi/\varkappa$ is the associated wavelength: (*blue line*) a Gaussian spectrum (cf. Flack et al. 2019) and (*gray lines*) the power law $E_{b'b'} \sim \varkappa^p$, with spectral slopes $p = -1.0$ and -1.5 (cf. Barros et al. 2018). The area under the premultiplied spectrum is $\int_0^\infty \varkappa E_{b'b'}\, \mathrm{d}(\log\lambda) = k_{\mathrm{rms}}^2$; the dashed line shows the viscous scale, ν/u_τ; and the dot-dashed line shows the outer scale, δ. (*b*) Illustration in spectral space of a hypothetical application roughness (*blue*, subscript a) scaled for laboratory measurements or numerical simulations (*red*, subscript s).

those of Yuan & Piomelli (2014b) that indicated that a loss in one may lead to a gain in the other. Interestingly, all these multiscale surfaces exhibit outer-layer similarity, suggesting indifference to spectral content. Presumably this may change if the surfaces were to contain substantial surface-elevation variations at in-plane wavelengths $\lambda \gtrsim \delta$, where heterogeneity (Section 5.2) or waviness (Section 5.4) effects could become active. However, surfaces with large-scale ($\lambda \gtrsim \delta$) spanwise heterogeneity could also recover an apparent outer-layer similarity, with noticeable departures only near $\lambda \approx \delta$ (Chung et al. 2018). Follow-up studies on multiscale surfaces by Barros & Christensen (2014) and Nikora et al. (2019) identified persistent secondary flows, suggesting that the surfaces tested had substantial surface-elevation variations near $\lambda \approx \delta$ (Section 5.2.2), although both studies also employed streamwise-repeated tiles, which have been proposed to play a role in accentuating these secondary flows (Nikora et al. 2019).

When evaluating multiscale roughness, it is useful to consider where the surface scales lie relative to the flow scales, δ and ν/u_τ. **Figure 7*a*** shows examples of premultiplied spectra of surface-elevation variation, $\varkappa E_{b'b'}$, where $\varkappa$ is an in-plane wavenumber (e.g., the streamwise wavenumber $\varkappa_x$ in the case of a 1D $\varkappa_x$-spectrum) and $\lambda \equiv 2\pi/\varkappa$, the corresponding wavelength. For the Gaussian spectrum, the spectral content of the surface-elevation variation is largely localized, but not for the power-law spectra. Computations and experiments impose further cutoffs. At the small-scale end, resolution must be considered due to either computational mesh spacing or surface-scanning and -manufacturing techniques. It is desirable that these cutoffs do not affect the flow, i.e., that they be located at wavelengths with limited surface-elevation variation, and left of the viscous $\lambda = \nu/u_\tau$ line in **Figure 7*a***, noting that fluid gaps smaller than $2\text{–}3\nu/u_\tau$ are not felt by the flow in the transitionally rough regime (MacDonald et al. 2016, Sharma & García-Mayoral 2020). In the fully rough regime, the Kolmogorov scale near the roughness would be the smallest to be resolved (e.g., Coceal et al. 2007). At the large-scale end, computational domain size, sample scan area, and replicated tile size can all impose limits on resolved large-scale surface-elevation variations. It is desirable for this upper limit to be beyond the spectral content of the surface. **Figure 7*b*** illustrates the challenges arising from scaling of replicated surfaces for laboratory experiments or numerical simulations. The application curve represents the surface-elevation spectrum of an original surface as observed in an application. The mean wavelength $\bar{\lambda}$ of this

Premultiplied spectrum of surface-elevation variation: $\varkappa E_{b'b'}$ is useful because the area under it in log λ coordinates is k_{rms}^2, where $E_{b'b'}$ is the spectrum of surface-elevation variation b', $\varkappa$ is an in-plane wavenumber, and $\lambda \equiv 2\pi/\varkappa$

surface can be obtained from a ratio of spectral moments (e.g., Townsin 2003), $\overline{\lambda}/(2\pi) \equiv m_0/m_1$, locating the centroid of the area under the premultiplied spectrum. For the application, the outer scale δ_a is much greater than the variance-containing part of the spectrum, $\approx\overline{\lambda}_a$. When testing an observed roughness in the laboratory or in a simulation, we must scale the surface to preserve inner scaling, represented by the scaled curve in **Figure 7*b***, which shows a 4×-scaled surface such that $\overline{\lambda}_s = \overline{\lambda}_a^+ \nu_s/u_{\tau s}$. However, since Reynolds numbers of scaled facilities are often smaller than in applications ($\delta_s u_{\tau s}/\nu_s \ll \delta_a u_{\tau a}/\nu_a$), this scaling results in reduced scale separation between outer and inner scales, even for $\delta_s \gg (k_{rms})_s$. For the case illustrated, the scaling resulted in substantial surface-elevation variation at $\lambda = \delta_s$. A similar scenario occurred for Nugroho et al. (2020) in scaling an observed ship hull surface for testing in a laboratory, with the resulting surface-elevation variation at $\lambda = \delta$ for the scaled surface leading to atypical roughness function behavior (Section 5.4).

Spectral moment: the nth spectral moment is given by $m_n \equiv \int_0^\infty \varkappa^n E_{h'h'}\,\mathrm{d}\varkappa$, where $E_{h'h'}$ is the spectrum of surface-elevation variation h' and $\varkappa$ is an in-plane wavenumber

Waviness regime: the low-*ES* surfaces for which the roughness function ΔU^+ does not approach the fully rough asymptote, $(1/\kappa)\ln k^+ + \text{constant}$

5.4. Wavy Roughness

Roughness topographies characterized by large in-plane wavelengths λ compared to roughness height k, i.e., wavy features, remain under-explored, with studies (Napoli et al. 2008, Schultz & Flack 2009, Nugroho et al. 2020) showing ΔU^+ of these low-*ES* surfaces lacking the typical dependence on k^+. In the LES study of multiscale surfaces created from the superposition of 2D sinusoids, Napoli et al. (2008) found that ΔU^+, the pressure-to-viscous drag partition, and the mean streamlines do not collapse with the roughness height k_a^+ but instead with a quantity they termed the effective slope, *ES* (Section 3.1.2.1). Notably, mean streamlines show attached flow for $ES \approx 0.05$, consistent with the dominance of viscous drag and flow separation for $ES \approx 0.15$, independent of k_a^+. Schultz & Flack (2009) carried out experiments over close-packed pyramids, finding that ΔU^+ increases with the viscous-scaled roughness height, k_t^+, toward fully rough behavior, but only for $ES > 0.35$. For pyramids with $ES < 0.35$, ΔU^+ appears independent of k_t^+, reminiscent of the study of Napoli et al. (2008). Schultz & Flack (2009) termed this the "waviness regime," in which ΔU^+ lacks the typical dependence on k^+. In this waviness regime, a doubling of the roughness height, k_t, at fixed unit Reynolds number, U_δ/ν, had a negligible effect on the drag of the surface. Nugroho et al. (2020) carried out experiments over 2.5× and 15× (scaled) replicas of in-service ship hull paint, which resembles an orange peel and has $ES \approx 0.089$. The 2.5× roughness showed the expected fully rough scaling of ΔU^+ with k_a^+, while the 15× roughness did not, despite both surfaces having matched *ES*. Nugroho et al. (2020) attributed this to a lack of scale separation between the boundary-layer thickness δ and the roughness wavelength $\overline{\lambda}$, as $\delta/\overline{\lambda}$ is approximately 1 for the 15× case and approximately 6 for the 2.5× case (cf. Section 5.3). Nugroho et al. (2020) reported spanwise variations of the streamwise flow up to $\approx 0.4\delta$ above the 15× roughness but not above the 2.5× roughness, with concomitant impact on outer-layer similarity. It is interesting that the cases termed wavy by Schultz & Flack (2009) have comparable $\delta/\lambda = 3$–6. More studies are needed to better understand the wavy regime, but the effect of low $ES \propto k/\lambda$ is difficult to isolate from the competing requirement of high δ/λ because $\delta/k \propto (\delta/\lambda)/ES$, and practically it is a struggle to maintain sufficiently high δ/k.

6. CONVECTIVE HEAT TRANSFER OVER ROUGHNESS

Roughness alters convective heat (and mass) transfer (Section 2, **Figure 1**). In forced convection, a log profile for Θ^+ similar to that for U^+ (Section 2.2) can be argued. The dimensional requirements for the log layer are that close to the wall ($y \ll \delta$), the flow is oblivious to the outer geometry, yet far above the direct effect of viscosity, roughness and, now, also diffusion (i.e., y^+, y/k, and $Pry^+ \gg 1$). Thus, the only relevant dimensionless group is $(y/\theta_\tau)(\mathrm{d}\Theta/\mathrm{d}y) = 1/\kappa_\theta$, where

κ_θ ($\approx$0.47) is generally different from κ for momentum. The log profile follows upon integration. The following are physically equivalent, but integration constants (log intercepts) vary depending on the y scaling (cf. Yaglom 1979):

$$\Theta_R^+ = (1/\kappa_\theta)\ln y^+ + A_\theta(Pr) - \Delta\Theta^+(k^+, Pr), \quad 11.$$

$$\Theta_R^+ = (1/\kappa_\theta)\ln(y/y_0) + St_k^{-1}(k^+, Pr), \quad 12.$$

$$\Theta_R^+ = (1/\kappa_\theta)\ln(y/y_{0\theta}), \quad 13.$$

$$\Theta_R^+ = (1/\kappa_\theta)\ln(y/k_s) + g(k^+, Pr). \quad 14.$$

In y^+ coordinates, the log intercept $A_\theta - \Delta\Theta^+$ is constructed such that the temperature shift is $\Delta\Theta^+ \equiv \Theta_S^+ - \Theta_R^+ = 0$ for smooth walls (k^+ and $Pr\,k^+ \ll 1$) (Yaglom 1979); $\Delta\Theta^+ > 0$ can be interpreted as heat-transfer augmentation. In y/y_0 coordinates, where y_0 is the roughness length for momentum, St_k^{-1} is the log intercept called the inverse roughness Stanton number (Kays & Crawford 1993). In meteorology, the roughness length for heat $y_{0\theta}$ is used (Brutsaert 1982). In y/k_s coordinates, the log intercept is g (Dipprey & Sabersky 1963). Thus, similar to knowing either ΔU^+, B, or y_0/k in terms of k^+ for drag, the problem reduces to knowing either $\Delta\Theta^+$, St_k^{-1}, $y_{0\theta}/k$, or g in terms of k^+ and Pr for heat transfer.

6.1. Fully Rough Heat Transfer

The main difference between convective heat transfer and drag for conventional roughness is the lack of a pressure-drag analog (Dipprey & Sabersky 1963, Owen & Thomson 1963) such that in the fully rough regime, $k_s^+ \gtrsim 70$ (and $Pr \gtrsim 1$), unlike τ_w, q_w does not scale with the inertial flow set by the roughness elements $y_0 \propto k$, but remains sensitive to molecular fluid properties ν and α. This means that the log intercept St_k^{-1} of Θ^+ in y/y_0 coordinates does not approach a constant but depends on k^+ (or k_s^+) and Pr. The power law $St_k^{-1} = (1/0.8)(k_s^+)^{0.2}Pr^{0.44}$ is typical (Kays & Crawford 1993). The exponents are based on a fit to the log intercept in y/k_s coordinates proposed by Dipprey & Sabersky (1963), $g = k_f(k_s^+)^p Pr^m = St_k^{-1} + (1/\kappa_\theta)\ln(k_s/y_0)$, where we have $k_f = 5.19$, $p = 0.20$, and $m = 0.44$ for granular close-packed roughness spanning $Pr = 1.20$–5.94 and $k_s^+ \approx$ 2–2,000. The prefactor k_f depends on roughness topography. Diverse values, $p = 0.2$–0.5 and $m = 0.44$–0.8, have been fitted to heat- and mass-transfer data for $Pr \gtrsim 1$ from laboratory experiments and meteorological observations (Brutsaert 1982, Kanda et al. 2007), with p, m, k_f, and the choice of log intercept sensitive to each other. Unlike ΔU^+, a preferred asymptotic form of St_k^{-1} or $\Delta\Theta^+$ is yet to emerge, with wide scatter (**Figure 8*a***) among models, as it has been difficult to directly test the underlying hypothesized mechanisms (e.g., Owen & Thomson 1963, Yaglom 1979, Brutsaert 1982). DNS data for 3D sinusoids at $Pr = 0.7$ up to $k_s^+ \approx 400$ (MacDonald et al. 2019) suggest that $\Delta\Theta^+$ approaches a constant, as in smooth-wall scaling behavior, but also show a slight decrease beyond $k_s^+ \approx 250$ (**Figure 8*a***). The DNS data for irregular roughness at $Pr = 1.0$ up to $k_s^+ \approx 100$ (Peeters & Sandham 2019) also seem to approach saturation (**Figure 8*a***).

6.2. Effect of Roughness Topography on Heat Transfer

As with drag, heat transfer depends on roughness topography. In general, appreciation of the influence of roughness topography on heat transfer currently lags that for drag, owing to a scarcity of systematic studies. Nonetheless, a comparison of a large number of engineered roughnesses is reviewed by Ligrani et al. (2003). A performance measure for heat transfer that accounts for drag

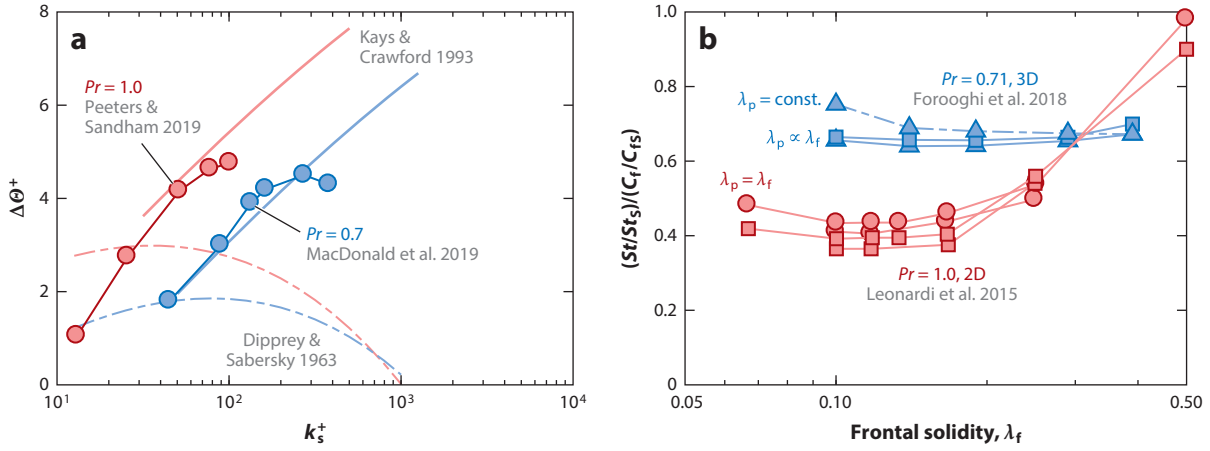

Figure 8

(*a*) Fully rough behavior of the temperature shift $\Delta\Theta^+$, showing scatter among models [using temperature log slope $\kappa_\theta = 0.47$ and intercepts $A_\theta(0.7) = 3.2$ and $A_\theta(1.0) = 6.0$] and direct numerical simulation (DNS) data comprising three-dimensional sinusoids (MacDonald et al. 2019) and irregular roughness (Peeters & Sandham 2019). (*b*) Fully rough Reynolds analogy efficiency $(St/St_S)/(C_f/C_{fS})$ from DNS data comprising transverse circular rods and square bars for $k_t^+ \approx 40$–150 (Leonardi et al. 2015) and irregular roughness for $k_{rms}^+ \approx 16$–31 (Forooghi et al. 2018), where k_t^+ and k_{rms}^+ are roughness Reynolds numbers, showing broad minima in the range $0.1 < \lambda_f < 0.3$, coinciding with the drag maxima (**Figure 5*a***), and a dependence on the choice of intersect in the frontal and plan solidity (λ_f, λ_p) space.

is the Reynolds analogy factor, $St/(C_f/2)$. This measure, relative to its smooth-wall value, defines an efficiency $(St/St_S)/(C_f/C_{fS})$ that has become common for comparing roughness topographies (e.g., Ligrani et al. 2003), noting that it depends mildly on δ^+ (Forooghi et al. 2018). For conventional surfaces, $(St/St_S)/(C_f/C_{fS})$ falls below unity, meaning that, percentage-wise, roughness increases drag more than heat transfer, except possibly for dimples (Ligrani et al. 2003) and riblets (Walsh & Weinstein 1979). DNS data for irregular roughness in the fully rough regime show that heat transfer is higher on the windward slopes, where unmixed fluid impinges with high temperature gradients, compared to the leeward slopes, where well-mixed fluid recirculates with low temperature gradients (Peeters & Sandham 2019). Because the frontal-area density λ_f controls these inertial flow regimes associated with impingement and recirculation (Grimmond & Oke 1999), heat transfer in the fully rough regime also shows broad peaks in the range $0.1 < \lambda_f < 0.3$ (Leonardi et al. 2015, Forooghi et al. 2018), coinciding with the λ_f of the well-known broad peaks in drag (**Figure 5*a***). The associated minima in the Reynolds analogy efficiency (**Figure 8*b***) tell us that the increase in heat transfer comes with an even higher increase in drag, most of it due to the pressure drag component (Leonardi et al. 2015). However, data suggest that this penalty is mitigated along the constant-λ_p intersect at low λ_f compared to the $\lambda_p \propto \lambda_f$ intersect (**Figure 8*b***). **Figure 8*b*** also shows clear differences in heat transfer performance between 2D and 3D roughness. Another principle is the similarity between the viscous drag component and heat transfer, as seen for sinusoidal roughness, except in reversed-flow regions (Leonardi et al. 2015, MacDonald et al. 2019), because, in the absence of internal heating, temperature cannot exceed its wall value. Hence, unlike viscous drag, heat can only transfer in one direction. We speculate that dimples and riblets augment heat more efficiently than smooth walls, $(St/St_S)/(C_f/C_{fS}) > 1$, by minimizing or eliminating pressure drag, while maximizing the local flow reversals (Chu & Karniadakis 1993, Ligrani et al. 2003) that increase the favorable dissimilarity between viscous drag and heat transfer.

7. SUMMARY POINTS AND FUTURE ISSUES

We are now seeing an abundance of detailed flow data across systematically varied roughnesses, allowing us to understand the physics of and limitations behind the correlations that relate topography to fluid dynamics. For roughnesses that obey outer-layer similarity, we should see, over time, increases in the reliability of predictions. For roughnesses that do not obey outer-layer similarity, such as heterogeneous roughness, new concepts and predictive tools beyond Moody-type diagrams are needed. Roughness multiphysics are practically important and will increasingly receive attention as they become accessible to high-fidelity studies. Some of these areas are already making headway, such as biofilms (e.g., Schultz et al. 2015, Murphy et al. 2018, Hartenberger 2019), roughness noise (e.g., Devenport et al. 2018), pressure gradients (e.g., Piomelli 2018), compressibility (e.g., Bowersox 2007), natural convection (e.g., Xie & Xia 2017), and curvature (e.g., Berghout et al. 2019).

SUMMARY POINTS

1. A primary goal of roughness research is to relate a surface topography, referenced by its size k, to the hydraulic scale k_s, which relates to drag.
2. Outer-layer similarity, particularly of the mean flow, is robust. All full-scale predictions rely on it, from Moody-type diagrams to large-eddy simulations. The behavior of a large number of roughnesses is well captured by it. If in doubt, check for outer-layer similarity at larger δ/k but fixed k^+.
3. Roughness-resolving direct numerical simulations at relevant δ^+ and δ/k and laboratory experiments with systematically varied roughness are now possible at manageable cost. Subsequently, our understanding of the topographical features that contribute to drag is improving. For example, we know that pits are less draggy than peaks (the effect of skewness is not symmetric with its sign).

FUTURE ISSUES

1. More systematic studies on irregular surfaces are needed to better understand how the equivalent sand-grain roughness height k_s, the wall offset d, and the roughness sublayer y_r depend on topographical parameters, e.g., root-mean-square roughness height k_{rms}, effective slope ES, and skewness Sk. It is especially informative to explore the extremities of the parameter space and better understand the effects of clustering and directionality.
2. Heterogeneity is relevant in applications, but how do we incorporate heterogeneity in predictive frameworks? For example, can we ascribe an equivalent homogeneous roughness that would still allow us to use a Moody chart?
3. In multiscale roughness, it is unclear if and how the scales should be filtered, and whether certain scales can be essentially explained by simpler models.
4. Low-order models beyond correlations (e.g., Gioia & Chakraborty 2006, Yang et al. 2016, Chavarin & Luhar 2020) that can run in seconds or minutes are also needed, not just for full-scale prediction, but also because they increase our confidence in prediction

by bridging the gap from a given roughness to the physics of simpler well-understood building-block flows.

5. Effort is required for predicting heat (and mass) transfer, in particular, for arriving at a consensus on the asymptotic form at high roughness Reynolds numbers at various Prandtl numbers and for improving our understanding of the influence of topography.

DISCLOSURE STATEMENT

The authors are not aware of any biases that might be perceived as affecting the objectivity of this review.

ACKNOWLEDGMENTS

The financial support of the Australian Research Council and the US Office of Naval Research is gratefully acknowledged. We thank the three anonymous referees, and Profs. M. Luhar and V. Nikora, for their help in improving this review.

LITERATURE CITED

Acharya M, Bornstein J, Escudier MP. 1986. Turbulent boundary layers on rough surfaces. *Exp. Fluids* 4:33–47

Amir M, Castro IP. 2011. Turbulence in rough-wall boundary layers: universality issues. *Exp. Fluids* 51:313–26

Anderson W, Barros J, Christensen KT, Awasthi A. 2015. Numerical and experimental study of mechanisms responsible for turbulent secondary flows in boundary layer flows over spanwise heterogeneous roughness. *J. Fluid Mech.* 768:316–47

Anderson W, Meneveau C. 2011. Dynamic roughness model for large-eddy simulation of turbulent flow over multiscale, fractal-like rough surfaces. *J. Fluid Mech.* 679:288–314

Antonia RA, Luxton RE. 1971. The response of a turbulent boundary layer to a step change in surface roughness. Part 1. Smooth to rough. *J. Fluid Mech.* 48:721–61

Antonia RA, Luxton RE. 1972. The response of a turbulent boundary layer to a step change in surface roughness. Part 2. Rough-to-smooth. *J. Fluid Mech.* 53:737–57

Barros JM, Christensen KT. 2014. Observations of turbulent secondary flows in a rough-wall turbulent boundary layer. *J. Fluid Mech.* 748:R1

Barros JM, Schultz MP, Flack KA. 2018. Measurements of skin-friction of systematically generated surface roughness. *Int. J. Heat Fluid Flow* 72:1–7

Bechert DW, Bruse M, Hage W, van der Hoeven JGT, Hoppe G. 1997. Experiments on drag-reducing surfaces and their optimization with an adjustable geometry. *J. Fluid Mech.* 338:59–87

Berghout P, Zhu X, Chung D, Verzicco R, Stevens RJAM, Lohse D. 2019. Direct numerical simulations of Taylor–Couette turbulence: the effects of sand grain roughness. *J. Fluid Mech.* 873:260–86

Bons JP. 2005. A critical assessment of Reynolds analogy for turbine flows. *J. Heat Transf.* 127:472–85

Bons JP, Taylor RP, McClain ST, Rivir RB. 2001. The many faces of turbine surface roughness. *J. Turbomach.* 123:739–48

Bowersox R. 2007. *Survey of high-speed rough wall boundary layers: invited presentation*. Paper presented at 37th AIAA Fluid Dynamics Conference, Miami, FL, AIAA Pap. 2007-3998

Bradshaw P. 2000. A note on "critical roughness height" and "transitional roughness." *Phys. Fluids* 12:1611–14

Breugem WP, Boersma BJ. 2005. Direct numerical simulations of turbulent flow over a permeable wall using a direct and a continuum approach. *Phys. Fluids* 17:025103

Breugem WP, Boersma BJ, Uittenbogaard RE. 2006. The influence of wall permeability on turbulent channel flow. *J. Fluid Mech.* 562:35–72

Brutsaert W. 1982. *Evaporation into the Atmosphere*. Dordrecht, Neth.: Springer
Busse A, Jelly TO. 2020. Influence of surface anisotropy on turbulent flow over irregular roughness. *Flow Turbul. Combust.* 104:331–54
Busse A, Lützner M, Sandham ND. 2015. Direct numerical simulation of turbulent flow over a rough surface based on a surface scan. *Comput. Fluids* 116:129–47
Castro IP. 2007. Rough-wall boundary layers: mean flow universality. *J. Fluid Mech.* 585:469–85
Chan L, MacDonald M, Chung D, Hutchins N, Ooi A. 2015. A systematic investigation of roughness height and wavelength in turbulent pipe flow in the transitionally rough regime. *J. Fluid Mech.* 771:743–77
Chan L, MacDonald M, Chung D, Hutchins N, Ooi A. 2018. Secondary motion in turbulent pipe flow with three-dimensional roughness. *J. Fluid Mech.* 854:5–33
Chan-Braun C, García-Villalba M, Uhlmann M. 2011. Force and torque acting on particles in a transitionally rough open-channel flow. *J. Fluid Mech.* 684:441–74
Chavarin A, Luhar M. 2020. Resolvent analysis for turbulent channel flow with riblets. *AIAA J.* 58:589–99
Cheng H, Castro IP. 2002. Near wall flow over urban-like roughness. *Bound.-Layer Meteorol.* 104:229–59
Chu DC, Karniadakis GE. 1993. A direct numerical simulation of laminar and turbulent flow over riblet-mounted surfaces. *J. Fluid Mech.* 250:1–42
Chung D, Chan L, MacDonald M, Hutchins N, Ooi A. 2015. A fast direct numerical simulation method for characterising hydraulic roughness. *J. Fluid Mech.* 773:418–31
Chung D, Monty JP, Hutchins N. 2018. Similarity and structure of wall turbulence with lateral wall shear stress variations. *J. Fluid Mech.* 847:591–613
Clauser FH. 1954. Turbulent boundary layers in adverse pressure gradients. *J. Aeronaut. Sci.* 21:91–108
Coceal O, Dobre A, Thomas TG, Belcher SE. 2007. Structure of turbulent flow over regular arrays of cubical roughness. *J. Fluid Mech.* 589:375–409
Colebrook CF. 1939. Turbulent flow in pipes, with particular reference to the transition region between the smooth and rough pipe laws. *J. Inst. Civ. Eng.* 11:133–56
Coles D. 1968. The young person's guide to the data. In *Proceedings of the AFOSR-IFP-Stanford Conference on Computation of Turbulent Boundary Layers*, Vol. 2, ed. DE Coles, EA Hirst, pp. 1–45. Stanford, CA: Dep. Mech. Eng.
Colombini M, Parker G. 1995. Longitudinal streaks. *J. Fluid Mech.* 304:161–83
Devenport W, Alexander N, Glegg S, Wang M. 2018. The sound of flow over rigid walls. *Annu. Rev. Fluid Mech.* 50:435–58
Dipprey DF, Sabersky RH. 1963. Heat and momentum transfer in smooth and rough tubes at various Prandtl numbers. *Int. J. Heat Mass Transf.* 6:329–53
Elliot WP. 1958. The growth of the atmospheric internal boundary layer. *Eos* 39:1048–54
Fadlun EA, Verzicco R, Orlandi P, Mohd-Yusof J. 2000. Combined immersed-boundary finite-difference methods for three-dimensional complex flow simulations. *J. Comput. Phys.* 161:35–60
Finnigan J. 2000. Turbulence in plant canopies. *Annu. Rev. Fluid Mech.* 32:519–71
Flack KA, Schultz MP. 2010. Review of hydraulic roughness scales in the fully rough regime. *J. Fluids Eng.* 132:041203
Flack KA, Schultz MP. 2014. Roughness effects on wall-bounded turbulent flows. *Phys. Fluids* 26:101305
Flack KA, Schultz MP, Barros JM. 2019. Skin friction measurements of a systematically-varied roughness: probing the role of roughness amplitude and skewness. *Flow Turbul. Combust.* 104:317–29
Flack KA, Schultz MP, Barros JM, Kim YC. 2016. Skin-friction behavior in the transitionally-rough regime. *Int. J. Heat Fluid Flow* 61:21–30
Flack KA, Schultz MP, Connelly JS. 2007. Examination of a critical roughness height for outer layer similarity. *Phys. Fluids* 19:095104
Flack KA, Schultz MP, Rose WB. 2012. The onset of roughness effects in the transitionally rough regime. *Int. J. Heat Fluid Flow* 35:160–67
Flack KA, Schultz MP, Shapiro TA. 2005. Experimental support for Townsend's Reynolds number similarity hypothesis on rough walls. *Phys. Fluids* 17:035102
Forooghi P, Stripf M, Frohnapfel B. 2018. A systematic study of turbulent heat transfer over rough walls. *Int. J. Heat Mass Transf.* 127:1157–68

Forooghi P, Stroh A, Magagnato F, Jakirlić S, Frohnapfel B. 2017. Toward a universal roughness correlation. *J. Fluids Eng.* 139:121201
García-Mayoral R, de Segura GG, Fairhall CT. 2019. The control of near-wall turbulence through surface texturing. *Fluid Dyn. Res.* 51:011410
Garratt JR. 1990. The internal boundary layer—a review. *Bound.-Layer Meteorol.* 50:171–203
Gatti D, von Deyn L, Forooghi P, Frohnapfel B. 2020. Do riblets exhibit fully rough behaviour? *Exp. Fluids* 61:81
Gioia G, Chakraborty P. 2006. Turbulent friction in rough pipes and the energy spectrum of the phenomenological theory. *Phys. Rev. Lett.* 96:044502
Granville PS. 1958. *The frictional resistance and turbulent boundary layer of rough surfaces*. Tech. Rep. 1579, Hydromech. Lab., David Taylor Model Basin, Bethesda, MD
Grigson C. 1992. Drag losses of new ships caused by hull finish. *J. Ship Res.* 36:182–96
Grimmond CS, Oke TR. 1999. Aerodynamic properties of urban areas derived from analysis of surface form. *J. Appl. Meteorol.* 38:1262–92
Hama FR. 1954. Boundary-layer characteristics for smooth and rough surfaces. *Trans. SNAME* 62:333–58
Hanson RE, Ganapathisubramani B. 2016. Development of turbulent boundary layers past a step change in wall roughness. *J. Fluid Mech.* 795:494–523
Hartenberger J. 2019. *Drag production of filamentous biofilm*. PhD Thesis, Univ. Mich., Ann Arbor
Hinze JO. 1967. Secondary currents in wall turbulence. *Phys. Fluids* 10:S122
Hong J, Katz J, Schultz MP. 2011. Near-wall turbulence statistics and flow structures over three-dimensional roughness in a turbulent channel flow. *J. Fluid Mech.* 667:1–37
Howell D, Behrends B. 2006. A review of surface roughness in antifouling coatings illustrating the importance of cutoff length. *Biofouling* 22:401–10
Hwang HG, Lee JH. 2018. Secondary flows in turbulent boundary layers over longitudinal surface roughness. *Phys. Rev. Fluids* 3:014608
IATA (Int. Air Transp. Assoc.). 2019. *Economic performance of the airline industry: 2019 end-year report*. Tech. Rep., Int. Air Transp. Assoc., Montréal
Ismail U, Zaki TA, Durbin PA. 2018. The effect of cube-roughened walls on the response of rough-to-smooth (RTS) turbulent channel flows. *Int. J. Heat Fluid Flow* 72:174–85
Jackson PS. 1981. On the displacement height in the logarithmic velocity profile. *J. Fluid Mech.* 111:15–25
Jelly TO, Busse A. 2018. Reynolds and dispersive shear stress contributions above highly skewed roughness. *J. Fluid Mech.* 852:710–24
Jiménez J. 2004. Turbulent flows over rough walls. *Annu. Rev. Fluid Mech.* 36:173–96
Johnson BE, Christensen KT. 2009. Turbulent flow over low-order models of highly irregular surface roughness. *AIAA J.* 47:1288–99
Kanda M, Kanega M, Kawai T, Moriwaki R, Sugawara H. 2007. Roughness lengths for momentum and heat derived from outdoor urban scale models. *J. Appl. Meteorol. Climatol.* 46:1067–79
Kays WM, Crawford ME. 1993. *Convective Heat and Mass Transfer*. New York: McGraw-Hill. 2nd ed.
Krogstad PÅ, Efros V. 2010. Rough wall skin friction measurements using a high resolution surface balance. *Int. J. Heat Fluid Flow* 31:429–33
Krogstad PÅ, Efros V. 2012. About turbulence statistics in the outer part of a boundary layer developing over two-dimensional surface roughness. *Phys. Fluids* 24:075112
Kuwata Y, Kawaguchi Y. 2019. Direct numerical simulation of turbulence over systematically varied irregular rough surfaces. *J. Fluid Mech.* 862:781–815
Langelandsvik LI, Kunkel GJ, Smits AJ. 2008. Flow in a commercial steel pipe. *J. Fluid Mech.* 595:323–39
Lee SH, Sung HJ. 2007. Direct numerical simulation of the turbulent boundary layer over a rod-roughened wall. *J. Fluid Mech.* 584:125–46
Leonardi S, Orlandi P, Antonia RA. 2007. Properties of d- and k-type roughness in a turbulent channel flow. *Phys. Fluids* 19:125101
Leonardi S, Orlandi P, Djenidi L, Antonia RA. 2015. Heat transfer in a turbulent channel flow with square bars or circular rods on one wall. *J. Fluid Mech.* 776:512–30
Leonardi S, Orlandi P, Smalley RJ, Djenidi L, Antonia RA. 2003. Direct numerical simulations of turbulent channel flow with transverse square bars on one wall. *J. Fluid Mech.* 491:229–38

Li M, de Silva CM, Rouhi A, Baidya R, Chung D, et al. 2019. Recovery of wall-shear stress to equilibrium flow conditions after a rough-to-smooth step change in turbulent boundary layers. *J. Fluid Mech.* 872:472–91
Ligrani PM, Oliveira MM, Blaskovich T. 2003. Comparison of heat transfer augmentation techniques. *AIAA J.* 41:337–62
Luchini P, Manzo F, Pozzi A. 1991. Resistance of a grooved surface to parallel flow and cross-flow. *J. Fluid Mech.* 228:87–109
Luhar M, Rominger J, Nepf H. 2008. Interaction between flow, transport and vegetation spatial structure. *Environ. Fluid Mech.* 8:423–39
MacDonald M, Chan L, Chung D, Hutchins N, Ooi A. 2016. Turbulent flow over transitionally rough surfaces with varying roughness densities. *J. Fluid Mech.* 804:130–61
MacDonald M, Chung D, Hutchins N, Chan L, Ooi A, García-Mayoral R. 2017. The minimal-span channel for rough-wall turbulent flows. *J. Fluid Mech.* 816:5–42
MacDonald M, Hutchins N, Chung D. 2019. Roughness effects in turbulent forced convection. *J. Fluid Mech.* 861:138–62
MacDonald M, Ooi A, García-Mayoral R, Hutchins N, Chung D. 2018. Direct numerical simulation of high aspect ratio spanwise-aligned bars. *J. Fluid Mech.* 843:126–55
Macdonald RW, Griffiths RF, Hall DJ. 1998. An improved method for the estimation of surface roughness of obstacle arrays. *Atmos. Environ.* 32:1857–64
Medjnoun T, Vanderwel C, Ganapathisubramani B. 2018. Characteristics of turbulent boundary layers over smooth surfaces with spanwise heterogeneities. *J. Fluid Mech.* 838:516–43
Mejia-Alvarez R, Christensen KT. 2010. Low-order representations of irregular surface roughness and their impact on a turbulent boundary layer. *Phys. Fluids* 22:015106
Mejia-Alvarez R, Christensen KT. 2013. Wall-parallel stereo particle-image velocimetry measurements in the roughness sublayer of turbulent flow overlying highly irregular roughness. *Phys. Fluids* 25:115109
Monty JP, Dogan E, Hanson R, Scardino AJ, Ganapathisubramani B, Hutchins N. 2016. An assessment of the ship drag penalty arising from light calcareous tubeworm fouling. *Biofouling* 32:451–64
Moody LF. 1944. Friction factors for pipe flow. *Trans. ASME* 66:671–84
Moyes AJ, Kostak HE, Cox CN, Kocian TS, Saric WS, et al. 2017. *Drag reduction initial conditions on various legacy fleet aircraft: surface roughness measurements*. Paper presented at 55th AIAA Aerospace Sciences Meeting, Grapevine, TX, AIAA Pap. 2017-0285
Murphy EAK, Barros JM, Schultz MP, Flack KA, Steppe CN, Reidenbach MA. 2018. Roughness effects of diatomaceous slime fouling on turbulent boundary layer hydrodynamics. *Biofouling* 34:976–88
Musker AJ. 1980. Universal roughness functions for naturally-occurring surfaces. *Trans. CSME* 6:1–6
Nagib HM, Chauhan KA. 2008. Variations of von Kármán coefficient in canonical flows. *Phys. Fluids* 20:101518
Napoli E, Armenio V, De Marchis M. 2008. The effect of the slope of irregularly distributed roughness elements on turbulent wall-bounded flows. *J. Fluid Mech.* 613:385–94
Nepf HM. 2012. Flow and transport in regions with aquatic vegetation. *Annu. Rev. Fluid Mech.* 44:123–42
Newton R, Chung D, Hutchins N. 2018. An experimental investigation into the breakdown of riblet drag reduction at post-optimal conditions. In *Proceedings of the 21st Australasian Fluid Mechanics Conference*, ed. TCW Lau, RM Kelso. Adelaide, Aust.: Australas. Fluid Mech. Soc.
Nikora V, Koll K, McLean S, Dittrich A, Aberle J. 2006. Zero-plane displacement for rough-bed open-channel flows. In *River Flow 2002: Proceedings of the International Conference on Fluvial Hydraulics*, ed. Y Zech, D Bousmar, pp. 83–92. Lisse, Neth.: Balkema
Nikora V, McEwan I, McLean S, Coleman S, Pokrajac D, Walters R. 2007. Double-averaging concept for rough-bed open-channel and overland flows: theoretical background. *J. Hydraul. Eng.* 133:873–83
Nikora VI, Stoesser T, Cameron SM, Stewart M, Papadopoulos K, et al. 2019. Friction factor decomposition for rough-wall flows: theoretical background and application to open-channel flows. *J. Fluid Mech.* 872:626–64
Nikuradse J. 1933. *Strömungsgesetze in rauhen Rohren*. VDI-Forschungsh. 361. Berlin: Ver. Dtsch. Ing.
Nugroho B, Hutchins N, Monty JP. 2013. Large-scale spanwise periodicity in a turbulent boundary layer induced by highly ordered and directional surface roughness. *Int. J. Heat Fluid Flow* 41:90–102
Nugroho B, Monty JP, Utama IKAP, Ganapathisubramani B, Hutchins N. 2020. Non *k*-type behaviour of roughness when in-plane wavelength approaches the boundary layer thickness. *J. Fluid Mech*. In press

Orlandi P, Sassun D, Leonardi S. 2016. DNS of conjugate heat transfer in presence of rough surfaces. *Int. J. Heat Mass Transf.* 100:250–66
Owen PR, Thomson WR. 1963. Heat transfer across rough surfaces. *J. Fluid Mech.* 15:321–34
Peeters JWR, Sandham ND. 2019. Turbulent heat transfer in channels with irregular roughness. *Int. J. Heat Mass Transf.* 138:454–67
Perry AE, Joubert PN. 1963. Rough-wall boundary layers in adverse pressure gradients. *J. Fluid Mech.* 17:193–211
Piomelli U. 2018. Recent advances in the numerical simulation of rough-wall boundary layers. *Phys. Chem. Earth* 113:63–72
Placidi M, Ganapathisubramani B. 2015. Effects of frontal and plan solidities on aerodynamic parameters and the roughness sublayer in turbulent boundary layers. *J. Fluid Mech.* 782:541–66
Pokrajac D, Campbell LJ, Nikora V, Manes C, McEwan I. 2007. Quadrant analysis of persistent spatial velocity perturbations over square-bar roughness. *Exp. Fluids* 42:413–23
Pokrajac D, Finnigan JJ, Manes C, McEwan I, Nikora V. 2006. On the definition of the shear velocity in rough bed open channel flows. In *River Flow 2006: Proceedings of the International Conference on Fluvial Hydraulics*, ed. RML Ferreira, ECTL Alves, JGAB Leal, AH Cardoso, pp. 89–98. London: Taylor & Francis
Prandtl L, Schlichting H. 1934. Das Widerstandsgesetz rauher Platten. *Werft Reeder. Hafen* 15(1):1–4
Pullin DI, Hutchins N, Chung D. 2017. Turbulent flow over a long flat plate with uniform roughness. *Phys. Rev. Fluids* 2:082601
Raupach MR. 1994. Simplified expressions for vegetation roughness length and zero-plane displacement as functions of canopy height and area index. *Bound.-Layer Meteorol.* 71:211–16
Raupach MR, Antonia RA, Rajagopalan S. 1991. Rough-wall turbulent boundary layers. *Appl. Mech. Rev.* 44:1–25
Raupach MR, Thom AS, Edwards I. 1980. A wind-tunnel study of turbulent flow close to regularly arrayed rough surfaces. *Bound.-Layer Meteorol.* 18:373–97
Rouhi A, Chung D, Hutchins N. 2019. Direct numerical simulation of open-channel flow over smooth-to-rough and rough-to-smooth step changes. *J. Fluid Mech.* 866:450–86
Sarakinos S, Busse A. 2019. Influence of spatial distribution of roughness elements on turbulent flow past a biofouled surface. In *Proceedings of the 11th International Symposium on Turbulence and Shear Flow Phenomena (TSFP11)*. **http://www.tsfp-conference.org/proceedings/2019/238.pdf**
Schlichting H. 1937. *Experimental investigation of the problem of surface roughness*. Tech. Memo. 823, Natl. Adv. Comm. Aeronaut., Washington, DC
Schultz MP, Bendick JA, Holm ER, Hertel WM. 2011. Economic impact of biofouling on a naval surface ship. *Biofouling* 27:87–98
Schultz MP, Flack KA. 2007. The rough-wall turbulent boundary layer from the hydraulically smooth to the fully rough regime. *J. Fluid Mech.* 580:381–405
Schultz MP, Flack KA. 2009. Turbulent boundary layers on a systematically varied rough wall. *Phys. Fluids* 21:015104
Schultz MP, Flack KA. 2013. Reynolds-number scaling of turbulent channel flow. *Phys. Fluids* 25:025104
Schultz MP, Walker JM, Steppe CN, Flack KA. 2015. Impact of diatomaceous biofilms on the frictional drag of fouling-release coatings. *Biofouling* 31:759–73
Sharma A, Garca-Mayoral R. 2020. Turbulent flows over dense filament canopies. *J. Fluid Mech.* 888:A2
Shockling MA, Allen JJ, Smits AJ. 2006. Roughness effects in turbulent pipe flow. *J. Fluid Mech.* 564:267–85
Sigal A, Danberg JE. 1990. New correlation of roughness density effect on the turbulent boundary layer. *AIAA J.* 28:554–56
Spalart PR, Garbaruk A, Howerton BM. 2017. *CFD analysis of an installation used to measure the skin-friction penalty of acoustic treatments*. Paper presented at 23rd AIAA/CEAS Aeroacoustics Conference, Denver, CO, AIAA Pap. 2017-3691
Spalart PR, McLean JD. 2011. Drag reduction: enticing turbulence, and then an industry. *Philos. Trans. R. Soc. A* 369:1556–69
Squire DT, Morrill-Winter C, Hutchins N, Schultz MP, Klewicki JC, Marusic I. 2016. Comparison of turbulent boundary layers over smooth and rough surfaces up to high Reynolds numbers. *J. Fluid Mech.* 795:210–40

Sridhar A, Pullin DI, Cheng W. 2017. Rough-wall turbulent boundary layers with constant skin friction. *J. Fluid Mech.* 818:26–45
Stevens RJAM, Meneveau C. 2017. Flow structure and turbulence in wind farms. *Annu. Rev. Fluid Mech.* 49:311–39
Stewart MT, Cameron SM, Nikora VI, Zampiron A, Marusic I. 2019. Hydraulic resistance in open-channel flows over self-affine rough beds. *J. Hydraul. Res.* 57:183–96
Stimpson CK, Snyder JC, Thole KA, Mongillo D. 2017. Scaling roughness effects on pressure loss and heat transfer of additively manufactured channels. *J. Turbomach.* 139:021003
Stroh A, Schäfer K, Frohnapfel B, Forooghi P. 2020. Rearrangement of secondary flow over spanwise heterogeneous roughness. *J. Fluid Mech.* 885:R5
Thakkar M, Busse A, Sandham ND. 2017. Surface correlations of hydrodynamic drag for transitionally rough engineering surfaces. *J. Turbul.* 18:138–69
Thakkar M, Busse A, Sandham ND. 2018. Direct numerical simulation of turbulent channel flow over a surrogate for Nikuradse-type roughness. *J. Fluid Mech.* 837:R1
Townsend AA. 1956. *The Structure of Turbulent Shear Flow*. Cambridge, UK: Cambridge Univ. Press
Townsin RL. 2003. The ship hull fouling penalty. *Biofouling* 19:9–15
van Rij JA, Belnap BJ, Ligrani PM. 2002. Analysis and experiments on three-dimensional and irregular surface roughness. *J. Fluids Eng.* 124:671–77
Vanderwel C, Ganapathisubramani B. 2015. Effects of spanwise spacing on large-scale secondary flows in rough-wall turbulent boundary layers. *J. Fluid Mech.* 774:R2
Voermans JJ, Ghisalberti M, Ivey GN. 2017. The variation of flow and turbulence across the sediment–water interface. *J. Fluid Mech.* 824:413–37
Volino RJ, Schultz MP. 2018. Determination of wall shear stress from mean velocity and Reynolds shear stress profiles. *Phys. Rev. Fluids* 3:034606
Walsh MJ, Weinstein LM. 1979. Drag and heat-transfer characteristics of small longitudinally ribbed surfaces. *AIAA J.* 17:770–71
Wangsawijaya DD, Baidya R, Chung D, Marusic I, Hutchins N. 2020. The effect of spanwise wavelength of surface heterogeneity on turbulent secondary flows. *J. Fluid Mech.* 894:A7
Womack KM, Meneveau C, Schultz MP. 2019. Comprehensive shear stress analysis of turbulent boundary layer profiles. *J. Fluid Mech.* 879:360–89
Xie YC, Xia KQ. 2017. Turbulent thermal convection over rough plates with varying roughness geometries. *J. Fluid Mech.* 825:573–99
Yaglom AM. 1979. Similarity laws for constant-pressure and pressure-gradient turbulent wall flows. *Annu. Rev. Fluid Mech.* 11:505–40
Yang J, Anderson W. 2018. Numerical study of turbulent channel flow over surfaces with variable spanwise heterogeneities: Topographically-driven secondary flows affect outer-layer similarity of turbulent length scales. *Flow Turbul. Combust.* 100:1–17
Yang XIA, Sadique J, Mittal R, Meneveau C. 2016. Exponential roughness layer and analytical model for turbulent boundary layer flow over rectangular-prism roughness elements. *J. Fluid Mech.* 789:127–65
Yuan J, Piomelli U. 2014a. Estimation and prediction of the roughness function on realistic surfaces. *J. Turbul.* 15:350–65
Yuan J, Piomelli U. 2014b. Roughness effects on the Reynolds stress budgets in near-wall turbulence. *J. Fluid Mech.* 760:R1
Zhu X, Verschoof RA, Bakhuis D, Huisman SG, Verzicco R, et al. 2018. Wall roughness induces asymptotic ultimate turbulence. *Nat. Phys.* 14:417–23